Large Chinese terrestrial carbon sink estimated from atmospheric CO_2 data

Jing Wang[1,2,3,4], Liang Feng[3,4], Paul I. Palmer[3,4,†], Yi Liu[1,2,‡], Shuangxi Fang[5,6,¥], Hartmut Bösch[7], Christopher W. O'Dell[8], Xiaoping Tang[9], Dongxu Yang[1,2], Lixin Liu[6], ChaoZong Xia[9]

1 Institute of Atmospheric Physics, Chinese Academy of Sciences, Beijing, China

2 University of Chinese Academy of Sciences, Beijing, China

3 National Centre for Earth Observation, University of Edinburgh, UK

4 School of GeoSciences, University of Edinburgh, UK

5 College of Environment, Zhejiang University of Technology, Hangzhou, China

6 Meteorological Observation Centre, China Meteorological Administration, Beijing, China

7 National Centre for Earth Observation, University of Leicester, UK

8 Colorado State University, Fort Collins, CO, USA

9 Academy of Forest Inventory and Planning, State Forestry Administration, Beijing, China

† Corresponding author 1: Paul Palmer, paul.palmer@ed.ac.uk

‡ Corresponding author 2：Yi Liu，liuyi@mail.iap.ac.cn

¥ Corresponding author 3: Shuangxi Fang, fangsx@cma.gov.cn

Limiting the rise in global mean temperatures relies on reducing carbon dioxide (CO_2) emissions and on the removal of CO_2 by land carbon sinks. China is currently the single largest emitter of CO_2, responsible for ~27% (~2.67 PgC/yr) of global fossil fuel emissions in 2017[1]. Current understanding of Chinese land biosphere fluxes has been hampered by sparse data coverage[2-4] resulting in a wide range of *a posteriori* flux estimates. Here, we present newly available atmospheric CO_2 mole fraction data measured from six sites across China during 2009-2016. Using these data, we estimate a Chinese land biosphere sink of -1.11±0.38 PgC/yr, equivalent to approximately 45% of annual estimated Chinese fossil fuel emissions in 2017. Our estimate reflects a previously underestimated land carbon sink over southwest China (Yunnan, Guizhou, and Guangxi provinces) throughout the year and over northeast China (especially Heilongjiang and Jilin provinces) during summer months. These provinces have established a pattern of rapid afforestation of progressively larger forested regions[5-6], with provincial forest areas increasing by 0.04-0.39x10^6ha/yr over the past 10-15 years. These large-scale changes reflect the expansion of fast-growing plantation forests that contribute to timber exports and the domestic production of paper[7]. Space-borne observations of vegetation greenness show a significant increase with time over this study period, supporting the timing and increase in the land carbon sink over these afforestation regions.

The global mass and growth of atmospheric CO_2 can be determined by surface-based measurements[8]. The largest anthropogenic emissions of CO_2 include fossil fuel combustion, cement production, and human-driven changes to land use[1]. Reconciliation of bottom-up emission estimates of these anthropogenic processes, accounting for widely assumed uncertainties, with atmospheric CO_2 measurements reveals a surprisingly invariant airborne fraction of 44±14%[9]. The remainder is absorbed by the ocean and land biosphere[10]. Sparse measurements of oceanic pCO_2, taking advantage of large-scale spatial-temporal correlations, allow estimation of ocean CO_2 fluxes[11]; although regional campaigns highlight large flux variations in successive years[12]. The residual of these mass balance terms yields the magnitude of the land biosphere carbon balance[10]. Current understanding of the land biosphere, encapsulated in numerical models, requires additional uptake to be reconciled with the data-driven residual term, even accounting for uncertainties[3]. And therein lies the crux of the challenge faced by the science and policy communities: effective mitigation of fossil fuel CO_2 emissions within a large-scale, dynamic natural carbon cycle that we do not quantitatively understand.

China overtook the United States in 2006 as the single largest emitter of CO_2 from fossil fuel combustion and cement production[13]. These emission estimates have large uncertainties[14] that translate into larger uncertainties for residual terrestrial biosphere flux estimates[2-3] (see Methods). Sparse *in situ* observations over China result in a large model spread of *a posteriori* terrestrial fluxes estimates[2,3,15], with values highly sensitive to available data[4].

Constraints on CO_2 flux estimates

In this study, we use newly available *in situ* CO_2 mole fraction data (collectively describing weekly flask and hourly continuous measurements) over China (see Data and SI; Extended Data Fig. 1) from 2009 to 2016 to show how these data can revise the provincial and national carbon balance of China. We corroborate our unexpected *a posteriori* flux estimates with independent satellite remote sensing measurements of vegetation greenness, soil water availability, *a posteriori* fluxes inferred from satellite column observations of CO_2, and with consecutive Chinese forest censuses.

We use several sources of data to investigate the Chinese carbon balance (see Methods and SI): *in situ* measurements of CO_2 mole fraction, satellite column observations of CO_2, leaf area index (LAI), normalized difference and enhanced vegetation indices (NDVI, EVI), liquid water equivalent thickness derived from gravity anomalies, and above ground biomass inferred from microwave measurements. The atmospheric data are interpreted using the GEOS-Chem atmospheric transport model coupled with a Bayesian inversion tool to infer CO_2 fluxes from the atmospheric data (see Data and Methods).

CO_2 fluxes inferred from atmospheric data

First, we use an atmospheric inversion to estimate the magnitude and distribution of land biosphere CO_2 fluxes over China (see Methods). Inversion SR-1, which uses only the ObsPack GLOBALVIEWplus data (Fig. 1a) provided by the Earth System Research Laboratory (ESRL) of the National Oceanic and Atmospheric Administration (NOAA), shows a CO_2 sink over most of China (Fig. 1b), mainly focused over central China, northeast China, and southern China. These data are consistent with a mean annual net uptake estimate for the terrestrial biosphere of -0.66±0.52 PgC/yr (2010—2016), varying from -0.52±0.54 PgC/yr in 2015 to -0.77±0.47 PgC/yr in 2016 (Fig. 1e, Table 1). We find the annual Chinese carbon sink

is mostly due to uptake during the growing season, particularly during June to August (Fig. 1f).

Including the Siberian tower data (see Data, Table S1) broadly increases CO_2 uptake over China and India. The additional Chinese sites (Extended Data Fig. 1), together with the Siberian data, in inversion SR-2 (Fig. 1a) have two major impacts on our understanding of the Chinese carbon budget. First, these data bring into sharper focus the distribution of Chinese CO_2 fluxes (Fig. 1c), increasing the net uptake over the southwest (mainly Yunnan, Guizhou, and Guangxi provinces), and increasing net emissions over the northeast (mainly Heilongjiang, Jilin and Liaoning provinces) relative to SR-1 (Fig. 1d). Second, the resulting uncertainties of the Chinese CO_2 budget are also much smaller than using only the NOAA ObsPack data (Fig. 1f, Fig. S6).

Table 1 reports annual CO_2 fluxes for China. Using inversion SR-2, we find the mean annual Chinese land biosphere sink is -1.11 ± 0.38 PgC/yr over 2010-2016. The magnitude of this sink term is 67.5% larger than the *a posteriori* values inferred from SR-1 for the same period (-0.66 ± 0.52 PgC/yr), with uncertainties reduced by about 27% (Fig. 1f, Table 1; Fig. S6). This revised sink term is substantially larger (i.e. more uptake) than many recent estimates[3-4,15-19] that cover various periods between 1980 to 2013 and inferred using different methods and data, including the inversion of atmospheric data (Table 1).

Our *a posteriori* estimate of CO_2 uptake over southwest China (18-30°N, 95-110°E) accounts for about 32% of the uptake over mainland China. We also find evidence of substantial year to year variability of carbon uptake across China (Figs. 2a and 2b), with the largest values during boreal summer months. As we discuss below this variation is at least partly due to the young age structure of this forest ecosystem[20-22] and variations in meteorology (Fig. S13). The relatively smaller uptake over northeast China (compared to SR-1) is due to the elevated sink during the growing season (Figs. 2c and 2d, Extended Data Fig. 2) that is compensated by emissions during the rest of the year.

Understanding the CO_2 flux distributions

In the absence of independent downwind data that are sensitive to our *a posteriori* changes in Chinese CO_2 fluxes, we also infer independent CO_2 flux estimates using

satellite column observations of CO_2 from the Japanese Greenhouse gases Observing SATellite (GOSAT)[23] and the NASA Orbiting Carbon Observatory (OCO-2) (see Data). Using these satellite data, we find that *a posteriori* CO_2 fluxes during the growing season (May to September) show larger uptake over central, northeast and southern parts of China than SR-1, consistent with the SR-2 inversion (Extended Data Fig. 3). Differences between these flux estimates can be partly explained by seasonal changes in clear-sky views (Extended Data Fig. 4) that are determined by cloud cover and aerosol loading. We find major gaps over China in winter, where the *a priori* information plays a larger role in the *a posteriori* solution (Extended Data Fig. 5).

Using reports from quinquennial Chinese forest inventories[24], we find that since the 1990s northeast and southwest China have experienced a period of rapid growth in forest area (Extended Data Fig. 6, Extended Data Table 1), reflecting national policies[25]. These findings are supported by remote sensing observations of land cover (Extended Data Fig. 7), vegetation indices (Fig. 3a, Extended Data Fig. 8, Figs. S11-S12) and above ground biomass (Fig. 3b) that show small but significant upward trends. A consequence of the rapid increase of afforestation during the last 30 years is that Chinese forests contain a large fraction of young and mid-aged trees (Extended Data Fig. 9), which are associated with a high rate of carbon sequestration[6,21,26,27].

The southwest region, in particular the Guangxi autonomous region, is populated by Eucalyptus, which is a fast growing and high-yielding tree species with high potential biomass carbon sequestration[28]. These eucalyptus plantations are irrigated and fertilized, factors that would need to be considered in the overall environmental value of this carbon sink. Correlative satellite data of leaf phenology and groundwater (Fig. 3, SI) clearly show upward trends that together are consistent with a progressively larger biological carbon sink. Because it is a managed ecosystem, the southwest region appears to be insensitive to wider changes in climate (Fig. S13-14), particularly during the 2009-2010 drought associated with reduced precipitation[29].

We have shown that using atmospheric CO_2 measurements collected at a small number of additional sites changes our understanding of the distribution of CO_2 fluxes over China. This reflects the sparse and uneven distribution of ground-based

measurements. Our use of satellite observations to verify *a posteriori* fluxes inferred from the *in situ* data heralds a new era in CO_2 monitoring.

References

1. Quere C L, et al. Global Carbon Budget 2018. *Earth Syst. Sci. Data.*, 10(4): 2141-2194 (2018).
2. Peylin, P. et al. (2013). Global atmospheric carbon budget: results from an ensemble of atmospheric CO_2 inversions. *Biogeosciences* **10,** 6699-6720 (2013).
3. Thompson, R. L. et al. Top–down assessment of the Asian carbon budget since the mid 1990s. *Nat. Commun.* **7,** 1-10 (2016).
4. Jiang, F., et al. A comprehensive estimate of recent carbon sinks in China using both top-down and bottom-up approaches. *Sci. Rep.* **6,** 1-9 (2016)
5. Pan, Y., et al. A large and persistent carbon sink in the world's forests. *Science* **333,** 988-993 (2011).
6. Zhang, Y., Yao, Y., Wang, X., Liu, Y., & Piao, S. Mapping spatial distribution of forest age in China. *Earth and space science **4**,* 108-116 (2017).
7. Williams, R. A. Mitigating biodiversity concerns in Eucalyptus plantations located in South China. *Journal of Biosciences and Medicines*, **3,** 1-8 (2015).
8. Ed Dlugokencky and Pieter Tans, NOAA/ESRL (www.esrl.noaa.gov/gmd/ccgg/trends/)
9. Barlow, J. M., Palmer, P. I., Bruhwiler, L. M., & Tans, P. Analysis of CO_2 mole fraction data: first evidence of large-scale changes in CO_2 uptake at high northern latitudes. *Atmos. Chem. Phys.* **15,** 13739-13758 (2015).
10. Schimel, D. S. et al. Recent patterns and mechanisms of carbon exchange by terrestrial ecosystems. *Nature* **414,** 169–172 (2001)
11. Takahashi, T. et al. Climatological mean and decadal change in surface ocean pCO_2, and net sea–air CO_2 flux over the global oceans. *Deep Sea Res. II.* **56,** 554-577 (2009).
12. Rödenbeck, C. et al. Data-based estimates of the ocean carbon sink variability–first results of the Surface Ocean pCO_2 Mapping intercomparison (SOCOM). *Biogeosciences*, **12,** 7251-7278 (2015).
13. Gregg, J. S., Andres, R. J. & Marland, G. China: Emissions pattern of the world leader in CO_2 emissions from fossil fuel consumption and cement production. Geophys. *Res. Lett.* **35,** 1-5 (2008).
14. Liu, Z., et al. Reduced carbon emission estimates from fossil fuel combustion and cement production in China. *Nature*, **524,** 335-338 (2015).
15. Piao, S. L. et al. The carbon budget of terrestrial ecosystems in East Asia over the last two decades. *Biogeosciences*, **9,** 3571-3586 (2012).
16. Piao, S., et al. The carbon balance of terrestrial ecosystems in China. Nature, 458(7241), 1009-1013(2009).
17. Tian, H., et al. Net exchanges of CO_2, CH_4, and N_2O between China's terrestrial ecosystems and the atmosphere and their contributions to global climate warming. *J. Geophys. Res. Atmos.***116**, G02011,1-13(2011).
18. Zhang, H., et al. Net terrestrial CO2 exchange over China during 2001–2010 estimated with an ensemble data assimilation system for atmospheric CO2. *J. Geophys. Res. Atmos.* **119(6)**, 3500-3515(2014).
19. Wang, Q., et al. Primary estimation of Chinese terrestrial carbon sequestration during 2001-2010. *Sci. Bull.* **60(6)**, 577-590(2015).
20. Fang, J. Y., Chen, A. P., Peng, C. H., Zhao, S. Q. & Ci, L. Changes in forest biomass carbon storage in China between 1949 and 1998. *Science* **292,** 2320-2322 (2001).
21. Pan, Y., Luo, T., Birdsey, R., Hom, J., & Melillo, J. New estimates of carbon storage and sequestration in China's forests: effects of age–class and method on inventory-based carbon estimation. *Clim. Change* **67,** 211-236 (2004).

22. Pan, Y., et al. A large and persistent carbon sink in the world's forests. *Science* **333,** 988-993 (2011).
23. Yokota, T. et al. Global concentrations of CO_2 and CH_4 retrieved from GOSAT: First preliminary results. *Sola*, **5,** 160-163 (2009).
24. Zeng, W., Tomppo, E., Healey, S. P., & Gadow, K. V. The national forest inventory in China: history-results-international context. *Forest Ecosystems*, **2,** 1-16 (2015).
25. Liu, J., Li, S., Ouyang, Z., Tam, C., & Chen, X. Ecological and socioeconomic effects of China's policies for ecosystem services. *PNAS*, **105,** 9477-9482 (2008).
26. Wang, S. et al. Relationships between net primary productivity and stand age for several forest types and their influence on China's carbon balance. *J. Environ. Manage.* **92,** 1651-1662 (2011).
27. Yu, Y. et al. Influence of site index on the relationship between forest net primary productivity and stand age. *PloS one*, **12,** 1-20 (2017).
28. Du, H. et al. Carbon storage in a Eucalyptus plantation chronosequence in Southern China. *Forests*, **6,** 1763-1778 (2015).
29. Xu, K., Yang, D., Xu, X., & Lei, H. Copula based drought frequency analysis considering the spatio-temporal variability in Southwest China. *J. Hydrology*, **527,** 630-640 (2015).

Acknowledgements

JW acknowledges support by the Strategic Priority Research Program of Chinese Academy of Sciences (Grant #XDA17010100) and funding from the UK Natural Environmental Research Council (NERC) National Centre for Earth Observation (NCEO). LF, PIP and HB are supported by the NERC NCEO (Grant #NE/R016518/1). HB acknowledges funding from the ESA CCI and C3S projects. PIP also acknowledges funding from a Royal Society Wolfson Research Merit Award. YL is supported by the international partnership program of the Chinese Academy of Sciences (Grant #134111KYSB20170010). SF is supported by the National Key Research and Development Program of China (Grant #2017YFC0209700). DY is supported by the National Key Research and Development Program of China (Grant #2016YFA0600203). CWO was supported by subcontracts from the OCO-2 project at the NASA Jet Propulsion Laboratory. JW, LF, PIP, YL, HB, and DY gratefully acknowledge funding from the ESA-MOST Dragon 3 Cooperation Programme. We gratefully acknowledge all CO_2 ground observations contributors to the obspack_co2_1_GLOBALVIEWplus_v4.1_2018-10-29 and to NOAA ESRL for maintaining this database. We also acknowledge data provided by Hong Kong Observatory, the Japan-Russia Siberia Tall Tower Inland Observation Network, and the World Data Centre for Greenhouse Gases. The NDVI, EVI and LAI data were retrieved from the online Data Pool, courtesy of the NASA Land Processes

Distributed Active Archive Center (LP DAAC), USGS/Earth Resources Observation and Science (EROS) Center, Sioux Falls, South Dakota, https://lpdaac.usgs.gov/data_access/data_pool. We also thank Peter Somkuti for GOSAT SIF data and the broader GOSAT team who provided the L1 data.

Author Contributions

YL, PIP, and LF designed the research; SF and LL processed and evaluated the observed data; JW and LF performed the atmospheric inversion analysis and data analysis; XT and CX provided the national forest inventory data. All authors contributed to the interpretation of the data. PIP and JW led the writing of the paper.

Competing Interests

The authors declare no competing financial interests.

Additional information

Supplementary information is available for this paper.

Correspondence and request for materials should be addressed to Paul Palmer (paul.palmer@ed.ac.uk).

Methods

Data:

***In situ* CO_2 mole fraction observations.** We use (weekly) discrete flask air samples from 105 sites and (hourly) continuous observations from 52 sites that are part of the global atmospheric surface CO_2 observations network. These are currently described by the Observation Package (ObsPack)

obspack_co2_1_GLOBALVIEWplus_v4.1_2018-10-29 data product[30] from National Oceanic and Atmospheric Administration (NOAA) Earth System Research Laboratory (ESRL). We also use an additional Chinese data from World Data Centre for Greenhouse Gases (WDCGG) at Hok Tsui (HKG) provided by Hong Kong Observatory.

We use CO_2 mole fraction data from nine towers collected by the Japan-Russia Siberia Tall Tower Inland Observation Network (JR-STATION; Table S1, Extended Data Fig.1) over Siberia from 2009-2016[31-32]. We also use weekly flask measurements and hourly continuous CO_2 mole fraction measurements during 2009-2016 of six new regional background sites over China (Longfengshan, Shangdianzi, Linan, Shangri-La, Jinsha, and Akedala) (Table S2, Extended Data Fig. 1) are operated by the China Meteorological Administration[33-34]. Further details about these CO_2 observations are in the SI.

GOSAT observations. We use column CO_2 data collected by the Japanese Greenhouse gases Observing SATellite (GOSAT), launched in January 2009 in a sun-synchronous orbit with a local overpass time over China around 13:00[35]. We use total column CO_2 (XCO_2) full-physics retrievals from GOSAT: v7.3 data product from the Atmospheric CO_2 Observations from Space (ACOS) from the Jet Propulsion Laboratory[38].

OCO-2 observations. We use column CO_2 data collected by NASA's Orbiting Carbon Observatory (OCO-2), launched in July 2014 in a sun-synchronous orbit with a local crossing time over China around 13:30[37]. We use bias-corrected OCO-2 V8r data[38] in this study. We use only nadir observations over land with a warning level <12. After considering observation error correlations we have thinned the data with a frequency of 0.1Hz, corresponding to an approximate distance of 75 km between successive measurements.

Normalized Difference Vegetation Index (NDVI) and Enhanced Vegetation Index (EVI) represent composite property of leaf area, chlorophyll and canopy structure. We use MOD13C2 (MODIS/Terra Vegetation Indices Monthly L3 Global 0.05° CMG V006)[39] to get NDVI AND EVI information. The data are only retained with pixel reliability values masked as good data ("0") or marginal data ("1").

Gravity Recovery and climate experiment (GRACE) provides information about changes in the water column[40-42]. Rooting depths of Chinese terrestrial ecosystems will likely be sufficiently deep that we cannot establish a direct and immediate relationship between vegetation and changes in precipitation. Changes in gravity due to changes in water column depth provide a much stronger relationship with vegetation access to water. We use the surface mass change data based on the RL05 spherical harmonics from CSR (Center for Space Research at University of Texas, Austin), JPL (Jet Propulsion Laboratory) and GFZ (Geoforschungs Zentrum Potsdam). The three different processing groups chose different parameters and solution strategies when deriving month-to-month gravity field variations from GRACE observations. We use the ensemble mean of the three data fields and multiply the data by the provided scaling grid. Data are available from http://grace.jpl.nasa.gov.

Above-ground Biomass Carbon (ABC). We use ABC estimates (1993-2012) based on harmonized vegetative optical depth data for 1993 onwards derived from a series of passive microwave satellite sensors[43]. These sensors include the Special Sensor Microwave Imager (SSM/I), Advanced Microwave Scanning Radiometer for Earth Observation System (AMSR-E), FengYun-3B Microwave Radiometer Imager (MWRI) and Windsat. Data are available from http://www.wenfo.org/wald/global-biomass

Models:

To describe the relationship between surface fluxes of CO_2 and atmospheric CO_2 we use the GEOS-Chem global 3-D chemistry transport model (v9.02). For our

experiments we run GEOS-Chem with a horizontal resolution of 4° (latitude) ×5° (longitude), driven by the GEOS-5 (GEOS-FP from 2013) meteorological analyses from the Global Modeling and Assimilation Office Global Circulation Model based at NASA Goddard Space Flight Centre.

To describe atmospheric CO_2, we use well-established emission inventories as our *a priori* flux estimates: 1) weekly biomass burning emissions[44]; 2) monthly fossil fuel emissions[45-47](we use 88% of ODIAC fossil fuel[45-46] inventory in this study, details in SI); 3) monthly climatological ocean fluxes[11]; and 4) three-hourly terrestrial biosphere fluxes[48].

We use an ensemble Kalman Filter (EnKF) framework[49-51] to infer CO_2 fluxes from the *in situ* or space-based measurements of atmospheric CO_2 concentrations. Surface flux $f^a(x,t)$ [kg/m^2/s] at location *x* and time *t* is given by[49,51]:

$$f^a(x,t) = f^0(x,t) + \sum_i^N c_i BF_i(x,t),$$

where $f^0(x,t)$ describes the *a priori* estimates [kg/m^2/s]. The basis function set $BF_i(x,t)$ is defined as the pulse-like (monthly) CO_2 fluxes over pre-defined geographic regions [kg/m^2/s]. For each individual basis function, we estimate the unitless scaling coefficient c_i by optimally fitting the model to observation data. The coefficients for the basis function set represent the state vector **c**.

We use a total of 792 monthly basis functions split between 317 oceanic regions and 475 land regions. These regions are based on established 22 regions in TransCom-3[52]. To infer Chinese CO_2 fluxes on a spatial resolution of 4° (latitude) ×5° (longitude) we further divide the Eurasia temperate region into 78 sub-regions.

We solve for the *a posteriori* state vector using the Kalman gain matrix $\mathbf{K}$:

$$\mathbf{c_a} = \mathbf{c}_f + \mathbf{K}\left(\boldsymbol{y}_{obs} - H\left(\mathbf{c}_f\right)\right),$$

where $\mathbf{c_a}$ and $\mathbf{c}_f$ represent the *a prior*i and *a posteriori* estimates, respectively; $\boldsymbol{y_{obs}}$ denotes the atmospheric CO_2 observations; and *H* describes the observation operator that relates surface fluxes to the observation data. In our case, *H* represents the GEOS-Chem model sampled at measurement locations, and in the case of satellite data also taking into account instrument sensitivity to CO_2.

We assume a 50% uncertainty for monthly land terrestrial fluxes, and 40% for monthly ocean fluxes[51]. We assume land (ocean) *a priori* fluxes are correlated with a correlation length of 500 (800) km.

We determine the terrestrial biosphere flux by subtracting the fossil fuel and cement production emission estimate (FF). This is a common approach[2-4,53], based on an assumption about our knowledge of FF flux. Consequently, our biosphere fluxes depend to a certain degree on what we assume for anthropogenic emissions (Table S3).

In addition to our control run (SR-2), we also report Chinese land biosphere fluxes that correspond to the ODIAC fossil fuel inventory[45-46]. We find that our total net *a posteriori* emissions of CO_2 over China (1.35±0.38 PgC/yr) are not significantly different to our control inversion (1.37±0.38 PgC/yr), suggesting that our *a posteriori* fluxes are robust. However, our *a posteriori* land biosphere fluxes represent a larger sink of CO_2 (-1.47±0.38 PgC/yr) compared to our control flux estimates (-1.11±0.38 PgC/yr). Our larger *a posteriori* sink estimate is expected since we are subtracting a larger FF flux from the net emission estimate. This calculation also provides a crude measure of the land biosphere flux uncertainty due to uncertainties in FF fluxes.

In the EnKF framework, the Kalman gain matrix $\mathbf{K}$ is approximated by[48]:

$$\mathbf{K} \approx \Delta\mathbf{C}\Delta\mathbf{Y}^{\mathrm{T}}[\Delta\mathbf{Y}\Delta\mathbf{Y}^{T} + \mathbf{R}]^{-\mathbf{1}},$$

where $\mathbf{R}$ is the observation error covariance matrix. $\Delta\mathbf{C}$ represents the ensemble of perturbations to the state vector that are used to construct the *a priori* error covariance, $\mathbf{P} \approx \Delta\mathbf{C}\Delta\mathbf{C}^{\mathrm{T}}$, where T denotes the matrix transpose[49]. To compare with observation, $\Delta\mathbf{C}$ is projected onto observation space using the observation operator $\Delta\mathbf{Y} = H(\Delta\mathbf{C})$. We assume no observation error correlations but include an additional 1.0 ppm uncertainty to the reported observation errors to account for model transport errors.

The methodology we use to estimate annual uncertainty estimates from the ensemble Kalman filter with a lagged window is described in detail in the SI.

Data availability. CO_2 mole fraction data from the Chinese sites used in this study are available at https://data.mendeley.com/datasets with name of 'CO_2 records from six sites in China'. Requests for further information about these data is directed to Shuangxi Fang (fangsx@cma.gov.cn). *NOTE to EDITOR: These data are now available via Extended Data Figure 1. They are also available via a private link: https://data.mendeley.com/datasets/w3bwmr6rfg/draft?a=074b5a77-d670-40bf-aff6-88802c174300. This link will be publicly available once the manuscript is published.*

Code availability. The community-led GEOS-Chem model of atmospheric chemistry and model is maintained centrally by Harvard University (http://acmg.seas.harvard.edu/geos/), and is available on request. The ensemble Kalman filter code is publicly available as PyOSSE (https://www.nceo.ac.uk/data-tools/atmospheric-tools/).

(Methods) References

30. Cooperative Global Atmospheric Data Integration Project; Multi-laboratory compilation of atmospheric carbon dioxide data for the period 1957-2016; obspack_co2_1_GLOBALVIEWplus_v3.2_2017_11_02; NOAA Earth System Research Laboratory, Global Monitoring Division. http://dx.doi.org/10.15138/G3704H (2017) Cooperative Global Atmospheric Data Integration Project; Multi-laboratory compilation of atmospheric carbon dioxide data for the period 1957-2017; obspack_co2_1_GLOBALVIEWplus_v4.1_2018_10_29; NOAA Earth System Research Laboratory, Global Monitoring Division. http://dx.doi.org/10.25925/20181026 (2018)
31. Sasakawa, M. et al. Continuous measurements of methane from a tower network over Siberia. *Tellus B*, **62,** 403-416 (2010).
32. Saeki, T. et al. Carbon flux estimation for Siberia by inverse modeling constrained by aircraft and tower CO_2 measurements. *J. Geophys. Res. Atmos.* **118,** 1100-1122 (2013).
33. Fang, S. X. *et al*. In situ measurement of atmospheric CO_2 at the four WMO/GAW stations in China. *Atmos. Chem. Phys*. **14,** 2541-2554 (2014).
34. Fang, S. X., Tans, P. P., Steinbacher, M., Zhou, L. X. & Luan, T. Comparison of the regional CO_2 mole fraction filtering approaches at a WMO/GAW regional station in China. *Atmos. Meas. Tech*. **8,** 5301-5313 (2015).
35. Kuze, A., Suto, H., Nakajima, M., and Hamazaki, T.: Thermal and near infrared sensor for carbon observation Fourier-transform spectrometer on the Greenhouse Gases Observing Satellite for greenhouse gases monitoring, Appl. Optics, 48, 6716–6733(2009).
36. OCO-2 Science Team/Michael Gunson, Annmarie Eldering (2016), ACOS GOSAT/TANSO-FTS ACOS Level 2 bias-corrected XCO2 and other select fields from the full-physics retrieval aggregated as daily files V7.3, Greenbelt, MD, USA, Goddard Earth Sciences Data and Information Services Center (GES DISC), Accessed: [*2017-10*], https://disc.gsfc.nasa.gov/datacollection/ACOS_L2_Lite_FP_7.3.html

37. Eldering, A., et al. The Orbiting Carbon Observatory-2 early science investigations of regional carbon dioxide fluxes. *Science*, **358**, eaam5745 (2017).
38. OCO-2 Science Team/Michael Gunson, Annmarie Eldering (2017), OCO-2 Level 2 bias-corrected XCO2 and other select fields from the full-physics retrieval aggregated as daily files, Retrospective processing V8r, Greenbelt, MD, USA, Goddard Earth Sciences Data and Information Services Center (GES DISC), doi: 10.5067/W8QGIYNKS3JC.
39. Didan, K. MOD13C2 MODIS/Terra Vegetation Indices Monthly L3 Global 0.05 Deg CMG V006, NASA EOSDIS Land Processes DAAC. https://doi.org/10.5067/modis/mod13c2.006 (2015).
40. Swenson, S., & Wahr, J. Post-processing removal of correlated errors in GRACE data. *Geophys. Res. Lett.* **33,** 1-4 (2006).
41. Swenson, S. C. GRACE monthly land water mass grids NETCDF RELEASE 5.0. Ver. 5.0. PO.DAAC, CA, USA. Dataset accessed [2017-09-27] at http://dx.doi.org/10.5067/TELND-NC005 (2012).
42. Landerer, F. W., & Swenson, S. C. Accuracy of scaled GRACE terrestrial water storage estimates. *Water. Resour. Res.* **48,** 1-11 (2012).
43. Liu, Y. Y., Van Dijk, A. I., De Jeu, R. A., Canadell, J. G., McCabe, M. F., Evans, J. P., & Wang, G. (2015). Recent reversal in loss of global terrestrial biomass. *Nat. Clim. Change* **5,** 470-474.
44. Van der Werf, G. R. et al. Global fire emissions and the contribution of deforestation, savanna, forest, agricultural, and peat fires (1997–2009). *Atmos. Chem. Phys.* **10,** 11707-11735 (2010).
45. Oda, T., & Maksyutov, S. A very high-resolution (1 km×1 km) global fossil fuel CO 2 emission inventory derived using a point source database and satellite observations of nighttime lights. *Atmos. Chem. Phys.* **11,** 543-556 (2011).
46. Oda, T., & Maksyutov, S., ODIAC Fossil Fuel CO_2 Emissions Dataset (ODIAC2016), Center for Global Environmental Research, National Institute for Environmental Studies, doi:10.17595/20170411.001. (Reference date: 2017/06/01) (2015).
47. Shan, Y., et al. China CO_2 emission accounts 1997-2015. *Sci.Data*, **5**, 170201(2018).
48. Olsen, S. C., & Randerson, J. T. Differences between surface and column atmospheric CO_2 and implications for carbon cycle research. *J. Geophys. Res. Atmos.* **109,** 1-11 (2004).
49. Feng, L., Palmer, P. I., Bösch, H., & Dance, S. Estimating surface CO 2 fluxes from space-borne CO_2 dry air mole fraction observations using an ensemble Kalman Filter. *Atmos. Chem. Phys*. **9,** 2619-2633 (2009).
50. Feng, L. et al. Evaluating a 3-D transport model of atmospheric CO_2 using ground-based, aircraft, and space-borne data. *Atmos. Chem. Phys*. **11,** 2789-2803(2011).
51. Feng, L., et al. Estimates of European uptake of CO_2 inferred from GOSAT XCO_2 retrievals: sensitivity to measurement bias inside and outside Europe. *Atmos. Chem. Phys*. **16,** 1289-1302 (2016).
52. Gurney, K. R., et al. Towards robust regional estimates of CO_2 sources and sinks using atmospheric transport models. *Nature*, **415**, 626-630(2002)
53. Saeki, T., & Patra, P. K. Implications of overestimated anthropogenic CO_2 emissions on East Asian and global land CO_2 flux inversion. *Geoscience Letters*, **4,** 9(2017).

Legends for Extended Data Figures and Table

Extended Data Fig. 1 *In situ* atmospheric CO_2 measurements across East Asia. **a** Map showing the location of atmospheric CO_2 measurement sites over East Asia used in our numerical experiments. Coloured dots represent individual measurement sites referred to by letter codes (Tables S1 and S2). Blue dots represent NOAA ObsPack stations, the cyan dot represents the HKG station from WDCGG, green dots represent Siberia stations, and red dots represent CMA regional background stations. **b—g** CO_2 mole fraction observations (ppm) at the six sites across China from 2009 to 2017 used in this study. Discrete (weekly) flask air samples, denoted by blue dots, and continuous (hourly) observations, denoted by black dots, are collected and analyzed by the China Meteorological Administration.

Extended Data Fig. 2 Monthly subcontinental Chinese CO_2 flux estimates. **a** map showing the sub-continental geographical regions over China where we report *a posteriori* CO_2 fluxes. Colours denote the proportion of each region that falls within mainland China. **b—g** monthly regional *a priori* and *a posteriori* biosphere CO_2 fluxes (PgC/month) over China during 2010—2016. *A posteriori* fluxes are inferred from data used in the SR-1 and SR-2 inversions (see main text). Vertical lines and the orange envelope denote *a priori* and *a posteriori* uncertainties.

Extended Data Fig. 3 Mean spatial distribution of *a priori* and *a posteriori* land biosphere CO_2 fluxes (gC/m^2/month) from May—September inferred from *in situ* and satellite observations of CO_2. **a** shows our *a priori* fluxes, and **b** and **c** show the *a posteriori* fluxes corresponding to inversions SR-1 and SR-2 (see main text) that use *in situ* data. **d** and **e** show *a posteriori* fluxes inferred from column observations of CO_2 from the Japanese Greenhouse gases Observing SATellite (GOSAT) and the NASA Orbiting Carbon Observatory (OCO-2), respectively. Flux estimates reported represent a temporal mean from 2010 to 2015, except for **e** that is only for 2015.

Extended Data Fig. 4 Seasonal distribution and magnitude of satellite retrievals of column CO_2 from December 2014 to November 2015. **a—d** show data from the Japanese Greenhouse gases Observing SATellite (GOSAT, v7.3 ACOS) and **e—h** show data from the NASA Orbiting Carbon Observatory (OCO-2, v8). See Data for further information.

Extended Data Fig. 5 *A priori* and *a posteriori* monthly biosphere CO_2 fluxes over China inferred from the GOSAT CO_2 column data and *in situ* data from 2010 to 2016. We also report *a posteriori* fluxes inferred from OCO-2 CO_2 column from September 2014 to December 2016. Vertical lines and shaded envelopes denote *a posteriori* uncertainties. Higher annual fluxes inferred from GOSAT and OCO-2 are due mainly to higher *a posteriori* fluxes during October to April when data coverage is sparse (Extended Data Fig. 4) and the fluxes are more influenced by *a priori* values.

Extended Data Fig. 6 Changes in forest area (10^6 ha), forest stocks (10^8 m^3), and forest coverage (%) over **a—f** six Chinese provinces and **g** China during 1973-2013. The x tick marks refer to the National Forest Inventory of China's State Forestry Administration: 1st (1973-1976), 2nd (1977-1981), 3rd (1984-1988), 4th (1989-1993), 5th (1994-1998), 6th (1999-2003), 7th (2004-2008), and 8th (2009-2013).

Extended Data Fig. 7 Forest cover change over China during the period 2002-2012. **a** shows how land cover changed with from 0 (1) denotes non-forest (forest) in both 2002 and 2012, 2 denotes conversion from non-forest to forest between 2002 and 2012, and 3 denote conversion from forest to non-forest between 2002 and 2012. **b** described the forest percentage change from 2002 to 2012. Data are presented on a 0.05^ox0.05^o spatial grid.

Extended Data Fig. 8 Multi-year mean of satellite observations of vegetation indices, **a** normalized difference vegetation index (NDVI), **b** enhanced vegetation index (EVI), and **c** leaf area index (LAI); **d** solar induced fluorescence (SIF); **e** gross primary production (GPP); **f** net photosynthesis (PSN); and **g** above-ground biomass carbon (ABC) (see SI text). The mean is over 2010-2012, inclusive, for ABC, and over 2010-2016 for the other data.

Extended Data Fig. 9 Forest area (**a-g**) and stock (**h-n**) of five age groups over six key forested provinces and China. Forest stands are divided into five age groups: young, mid-aged, near-mature, mature and over-mature. Data are taken from the 8th NFI.

Extended Data Table 1 Summary statistics calculated from the 6th to 8th (and 9th where available) National Forest Inventory of China's State Forestry Administration for China and six Chinese provinces.

559 # Figures

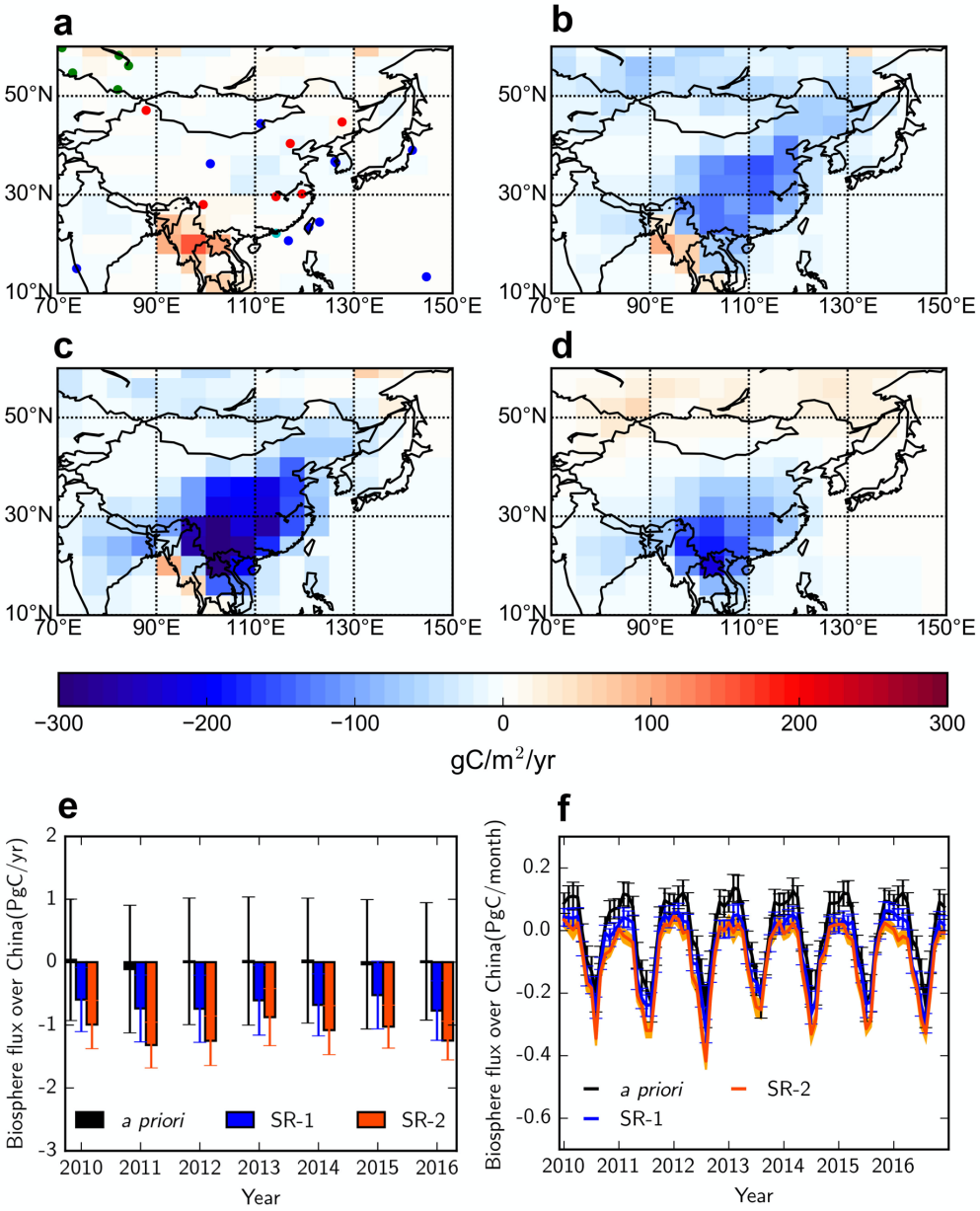

560

561 **Fig. 1** Chinese terrestrial biosphere CO_2 fluxes. Vertical lines and the yellow
562 envelope denote *a posteriori* uncertainties. Annual mean spatial distributions of CO_2
563 fluxes (gC/m^2/yr) 2010—2016 (inclusive) corresponding to **a** the *a priori* inventory
564 and *a posteriori* CO_2 fluxes corresponding to **b** SR-1 and **c** SR-2. f: difference
565 between SR-2 and SR-1 (gC/m^2/yr). **a** blue, cyan, green, and red dots denote NOAA
566 ObsPack stations, the HKG station from WDCGG, JR-STATION stations, and CMA
567 regional background stations, respectively. **e** Annual CO_2 fluxes (PgC/yr) from the *a*
568 *priori* inventory and *a posteriori* fluxes inferred from (SR-1) NOAA ObsPack CO_2
569 mole fraction measurements, and (SR-2) NOAA+Siberian+CMA+HKG CO_2 mole
570 fraction measurements from 2010 to 2016, inclusive; and **f** corresponding monthly
571 fluxes (PgC/month).

572

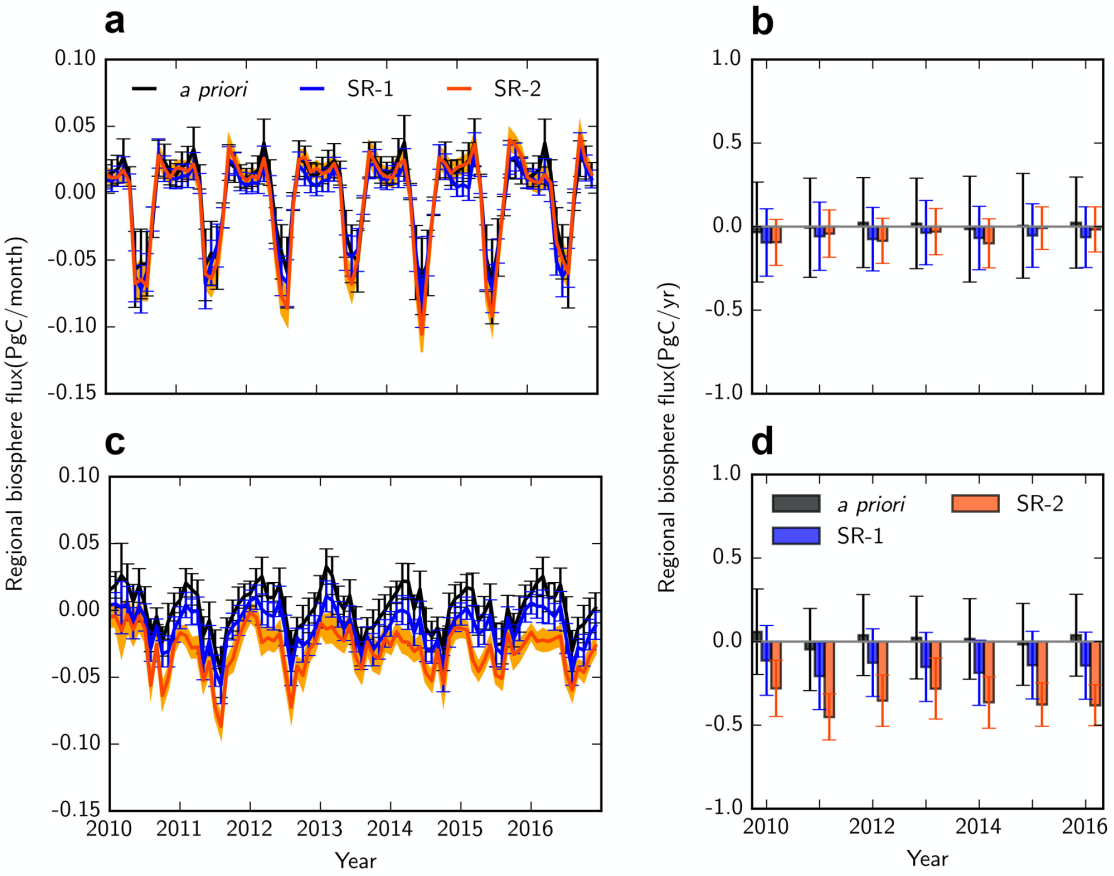

573

574 **Fig. 2** Terrestrial biosphere CO_2 fluxes over NEC and SWC. Monthly CO_2 fluxes
575 (PgC/month) from the *a priori* inventory and *a posteriori* fluxes inferred from SR-1
576 and SR-2 from 2010 to 2016 over **a** NEC and **c** SWC; and corresponding annual
577 fluxes (PgC/yr) over **b** NEC and **d** SWC. Vertical lines and the yellow envelope
578 denote *a posteriori* uncertainties. Northeastern China that lies within 38-54°N, 120-
579 135°E and southwestern China that lies within 18-30°N, 95-110°E

580

581

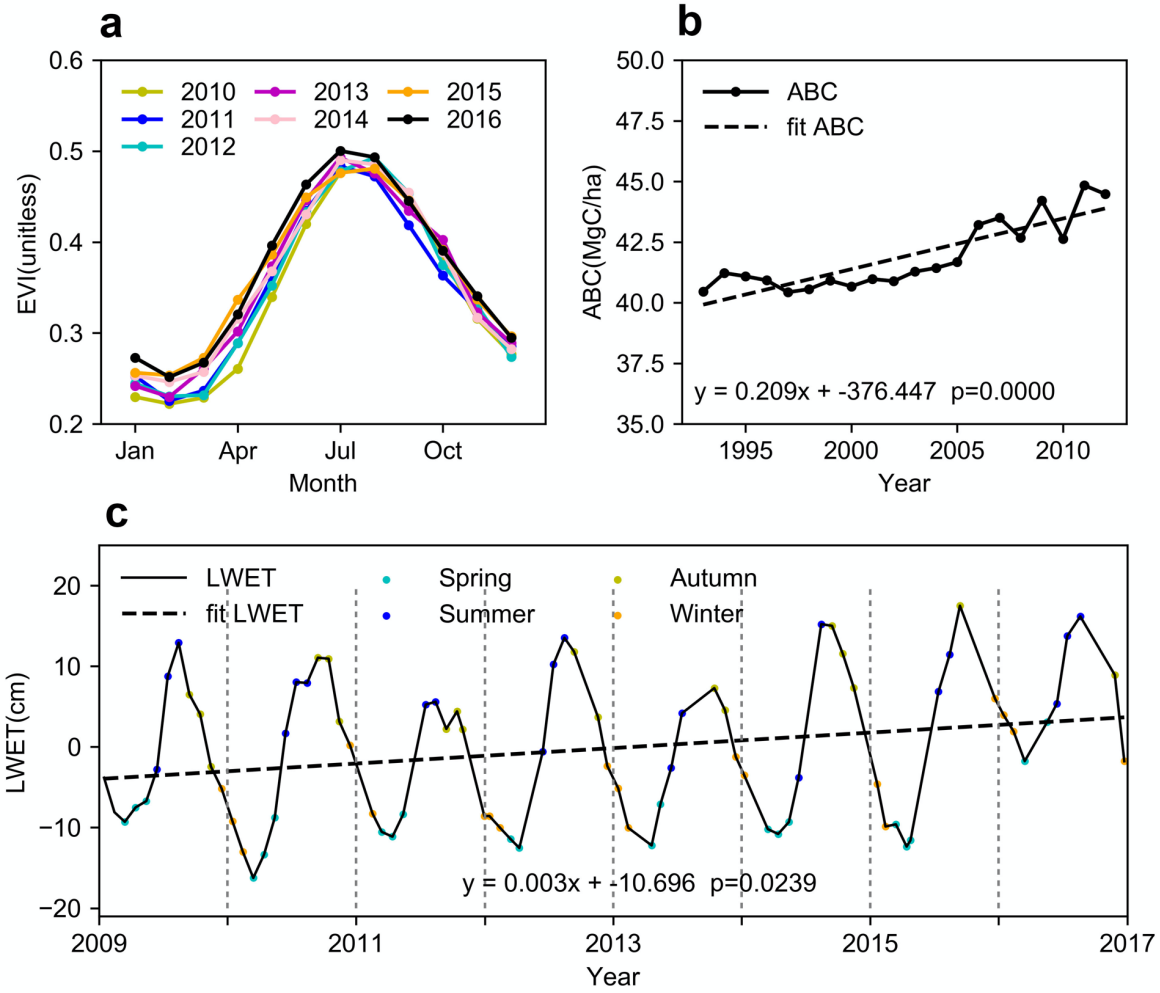

582

583 **Fig. 3** Satellite observations relating to vegetation growth. **a** leaf phenology, **b** above
584 ground biomass and **c** liquid water equivalent thickness over southwestern China
585 (18-30°N, 95-110°E). Data record lengths vary according to the sensor lifetime. **a**:
586 successive years (2010-2016) of superimposed monthly enhanced vegetation index
587 (EVI) from MODIS. **b** Above-ground biomass (MgC/ha) harmonized from several
588 sensors (1993-2012). **c** Liquid water equivalent thickness (cm) from the Gravity
589 Recovery And Climate Experiment (GRACE) (2009-2016). The linear best-fit lines
590 (dashed lines) and the associated p-values are shown inset of **b** and **c**. More
591 detailed data descriptions can be found in the SI.

Tables

Table 1 CO_2 fluxes (PgC/yr) of previous studies and this study over China and East Asia. In this study, inversion SR-1 denotes NOAA ObsPack *in situ* data (including one site over China); inversion SR-2 denotes *in situ* data from NOAA ObsPack, Siberia, and from China. Uncertainties represent one standard deviation from the mean value.

This study (PgC/yr)			**Previous Studies (PgC/yr)**			
Year	SR-1	SR-2	Method	Period	Carbon balance	Ref
2010	-0.60±0.51	-0.99±0.38	Inventory-satellite-based or process-based model estimation	1961-2005	-0.179★	17
2011	-0.74±0.53	-1.32±0.36		1980-1999	-0.177±0.073☆	16
2012	-0.74±0.53	-1.25±0.39		1990-2009	-0.224±0.141☆#	15
2013	-0.61±0.55	-0.87±0.45		2001-2010	-0.966☆	19
2014	-0.68±0.49	-1.08±0.39		2006-2009	-0.33☆	4
2015	-0.52±0.54	-1.03±0.34	Atmospheric inversion	1996-2005	-0.35±0.33★	16
2016	-0.77±0.47	-1.25±0.31		1990-2009	-0.270±0.507☆#	15
2010-2016 Mean	-0.66±0.52	-1.11±0.38		2001-2010	-0.33★	18
				2008-2012	-0.46 (-1.18 to -0.01)★#†	3
				2006-2009	-0.45	4

★ net CO_2 flux of terrestrial biosphere

☆ net CO_2 flux of terrestrial biosphere, including the contribution from the oxidation of reduced carbon.

East Asia, including China, Japan, North and South Korea, Mongolia.

† Ensemble model median and range.

Supplementary Information (SI)

Large Chinese terrestrial carbon sink estimated from atmospheric CO_2 data

Jing Wang[1,2,3,4], Liang Feng[3,4], Paul I. Palmer[3,4,†], Yi Liu[1,2,‡], Shuangxi Fang[5,6,¥], Hartmut Bösch[7], Christopher W. O'Dell[8], Xiaoping Tang[9], Dongxu Yang[1,2], Lixin Liu[6], ChaoZong Xia[9]

1 Institute of Atmospheric Physics, Chinese Academy of Sciences, Beijing, China

2 University of Chinese Academy of Sciences, Beijing, China

3 National Centre for Earth Observation, University of Edinburgh, UK

4 School of GeoSciences, University of Edinburgh, UK

5 College of Environment, Zhejiang University of Technology, Hangzhou, China

6 Meteorological Observation Centre, China Meteorological Administration, Beijing, China

7 National Centre for Earth Observation, University of Leicester, UK

8 Colorado State University, Fort Collins, CO, USA

9 Academy of Forest Inventory and Planning, State Forestry Administration, Beijing, China

† Corresponding author 1: Paul Palmer, paul.palmer@ed.ac.uk

‡ Corresponding author 2：Yi Liu， liuyi@mail.iap.ac.cn

¥ Corresponding author 3: Shuangxi Fang: fangsx@cma.gov.cn

The SI is organized into six sections:

1 Atmospheric CO_2 Data.....2

2 Atmospheric Transport Model and ensemble Kalman Filter.....9

3 Results.....12

4 Forest Data over China.....25

5 Comparison between *in situ* and satellite measurements inversion.....32

6 References.....33

1 Atmospheric CO_2 Data

NOAA/ESRL ObsPack database

We use discrete (weekly) flask air samples from 105 sites and continuous (hourly) observations from 52 sites that are part of the global atmospheric surface CO_2 observations network. These are currently described by the Observation Package (ObsPack) obspack_co2_1_GLOBALVIEWplus_v4.1_2018-10-29 data product (ObsPack, 2018) from National Oceanic and Atmospheric Administration (NOAA) Earth System Research Laboratory (ESRL). We use these data to estimate large-scale CO_2 fluxes that represent upwind boundary conditions for our China study region. We use weekly flask and hourly surface observed CO_2 data provided by NOAA/ESRL, depending on data availability at each site. The ObsPack data product includes NOAA flask measurements at two Chinese sites (Extended Data Figure 1): Mt. Waliguan (WLG) and Shangdianzi (SDZ). The China Meteorological Administration (CMA) collect collocated CO_2 flask measurements at WLG and SDZ. WLG is located in the northeastern part of the Tibetan Plateau in western China. The station is situated far from industrial and populated centres, providing atmospheric information about emissions from the Eurasian continent (Zhou et al., 2004, 2005). The SDZ station is located 150 km northeast of Beijing (Fang et al., 2014) and provides a constraint on fluxes over the north China plain.

WDCGG network

We also use additional Chinese data at Hok Tsui (HKG) provided by Hong Kong Observatory (Fung et al, 2010) and accessed from the World Data Centre for Greenhouse Gases (WDCGG). HKG is situated at Hok Tsui Peninsular at the south eastern coast of Hong Kong Island (22°12'N, 114 °15'E, 60 m.a.s.l.), approximately 20 km from the urban centre of Hong Kong. There is no major road or settlement within 3 km of HKG, and therefore this site is considered to be representative of the larger-scale Pearl River Delta region.

JR-STATION network

We use CO_2 mole fraction data from the Japan-Russia Siberia Tall Tower Inland Observation Network (JR-STATION; Table S1, Extended Data Figure 1) over 2009-2016 (Sasakawa et al., 2010, 2013; Watai et al., 2010). We use these data to provide additional constraints to boreal Eurasia CO_2 fluxes.

The network was constructed by the Center for Global Environmental Research at the Japanese National Institute for Environmental Studies with the cooperation of the Russian Academy of Science. It includes eight towers over western Siberia and one in eastern Siberia at Yakutsk (Extended Data Figure 1). A nondispersive infrared (NDIR) analyser (LI-820, LI-COR, USA) is used to measure CO_2 mole fraction. These CO_2 observations data were calibrated against NIES 09 CO_2 scale.

For our experiments we use hourly data collected during 13:00-17:00 local time when we expect the atmosphere is well mixed and representative of a large geographical region (Saeki et al., 2013; Sasakawa et al., 2010).

Identifying Code	Location	Latitude	Longitude	Altitude (m)	Sampling height (m)
BRZ	Berezorechka	56.15° N	84.33° E	150	5,20,40,80
KRS	Karasevoe	58.25° N	82.42° E	50	35,67
IGR	Igrim	63.19° N	64.42° E	25	24,47
NOY	Noyabrsk	63.43° N	75.78° E	100	21,43
DEM	Demyanskoe	59.79° N	70.87° E	75	45,63
SVV	Savvushka	51.33° N	82.13° E	400	27,52
AZV	Azovo	54.71° N	73.03° E	100	29,50
VGN	Vaganovo	54.50° N	62.32° E	200	42,85
YAK	Yakutsk	62.09° N	129.36° E	130	11,70

Table S1 Atmospheric CO_2 sites over Siberia (JR-STATION) used in our calculations.

China Meteorological Administration *in situ* observation network over China

The China Meteorological Administration (CMA) is responsible for greenhouse gases observations under the framework of World Meteorological Organization/Global Atmosphere Watch programme (WMO/GAW).

We use hourly or weekly CO_2 data from 2009-2016 at seven stations in CMA, including one WMO/GAW global station, three WMO/GAW regional stations, and three CMA background stations. Location of the seven stations is illustrated in Extended Data Figure 1, Table S2.

Identifying Code	Location	Latitude	Longitude	Altitude (m)	Sampling height(m)	Representation area
WLG	Mt.Waliguan	36.12° N	100.06° E	3816.0	10, 80	Northeastern of the Tibetan Plateau
SDZ	Shangdianzi	40.65° N	117.12° E	293.3	10, 80	The North China Plain
LFS	Longfengshan	44.73° N	127.60° E	330.5	10, 80	Northeastern Plain
LAN	Lin'an	30.30° N	119.72° E	138.6	10, 50	Yangtze River Delta Economic Zone
SL	Shangri-La	28.00° N	99.40° E	3580.0	5*, 10, 50	southwest of China
JS	Jinsha	29.63 ° N	114.22 ° E	750.0	5*	Jianghan plain, Centre of China
AKDL	Akedala	47.10° N	87.93° E	562.0	5*	Junggar Basin, northwest of China

Table S2 Atmospheric CO_2 sites over mainland China used in our calculations. Sampling heights marked by an asterisk correspond to flask samples.

The Waliguan Baseline Observatory is the only WMO/GAW global atmospheric background station in China and also the only global atmospheric background station in inland Eurasia. The observatory is built on the top of mountain Waliguan in the northeast of the Tibet plateau. Greenhouse gases measurements from this site provide essential information on sources and sinks from within the Eurasian continent because of its unique location. The observed data at the site is also submitted to World Data Centre of Greenhouse Gases (WDCGG) and used for many

scientific products (e.g., Global View database, WMO/GAW GHGs bulletin).

The LAN station is located at the centre of the Yangtze Delta area, 50 km from Hangzhou (the capital of Zheijang province) and 150 km from Shanghai. The Yangtze Delta economic zone represents one of the largest economic centres in China. The LFS station is in Northeast China, 175 km Southeast of Harbin City (the capital of Heilongjiang province) and provides a constraint on fluxes originating from the Northeastern Plain. The SDZ station is located 150 km northeast of Beijing (the capital of China) and provides a constraint on fluxes from the north China plain. The SL station is situated in Southwest China, 30 km north of Shangri-La county and 460 km from Kunming (the capital of Yunnan province). It resides in the transition zone of the Yunnan-Guizhou Plateau and the Tibetan Plateau. The JS station is located in the Jianghan plain located in the centre of China. AKDL is in the Xinjiang autonomous region in Northwest China and provides a constraint on the Gobi wetlands that reside between grassland and sparsely vegetated regions.

Instruments With the exception of JS and AKDL, all stations continuously measure CO_2 mole fractions using cavity ring-down spectroscopy (CRDS) analysers. The model of instruments was initially G1301 (Picarro Inc. USA), which we upgraded in 2015 to G2401 (Picarro Inc. USA).

Picarro CRDS instruments are commonly used by the global GHG measurement community because they have been proven suitable for making precise measurement of CO_2 mole fractions. The analysers have a highly linear response and are very stable (Crosson, 2008).

Figure S1 shows a schematic of the analytical system at Chinese stations. Ambient air is delivered to the instrument by a vacuum pump (N022, KNF Neuberger, Germany) via a dedicated 10 mm o.d. sampling line (Synflex 1300 tubing, Eaton, USA) and via a polytetrafluoroethylene (PTFE) 7 μm filter. The filtered ambient air is then pressurized to 1 atm and dried to a dew point of approximately - 60 °C by passing it through a glass trap submerged in a -70 °C ethanol bath (MC480D1, SP Industries, USA). An automated sampling module equipped with a VICI 8 port multi-position valve has been designed to sample from separate gas streams (standard gas cylinders, described below, and filtered ambient air). The residence time of the air from the top of the inlet to the analysers is less than 60 s. Further details about the measurement strategy are described by Fang et al. (2014).

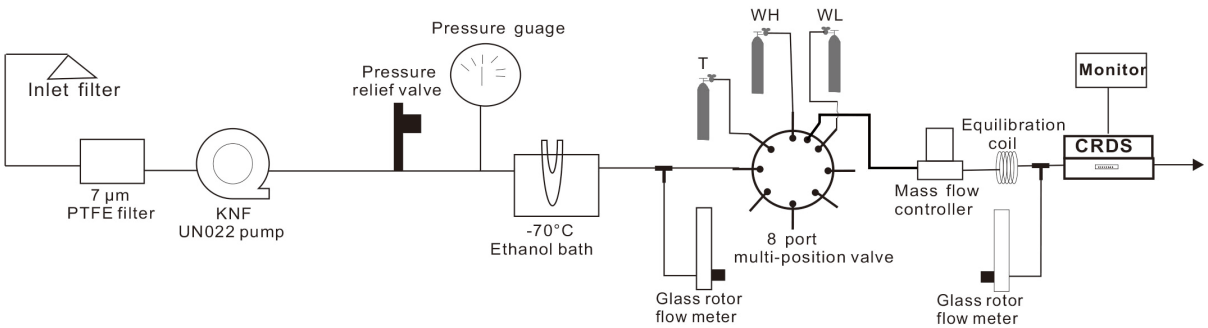

Figure S1 Schematic of the CRDS *in situ* observation system. WH denotes Working High standard, WL denotes Working Low standard, and T denotes Target gas.

The CO_2 mole fractions at JS and AKDL are collected as part of a larger discrete

flask sampling programme in China (with eight stations), similar to the NOAA flask program (Dlugokencky et al., 1994). Two samples are collected in series using glass flasks and a portable battery powered sampling apparatus with a 5 m (a.g.l.) intake height. Weekly flask samples are collected at JS and AKDL and shipped to Beijing where they are analysed for CO_2. The CO_2 in flask samples are analysed by a Picarro G2301 (Picarro Inc. USA) system with a flow rate of 150 mL min^{-1}. The repeatability of flask-Picarro system is approximately 0.1 ppm.

Calibration The *in situ* CO_2 observation systems are routinely calibrated against the standards propagated by the WMO/GAW CO_2 Central Calibration Laboratory operated by NOAA/ESRL using the WMO X2007 scale (Zhao et al., 1997; Zhao and Tans, 2006). Carbon dioxide mole fractions are referenced to a Working High (WH) and a Working Low standard (WL) by using a linear two-point fit through the most recent standard gas measurements (WH & WL). Additionally, a calibrated cylinder filled with compressed ambient air is used as a target gas (T) to check the precision and stability of the system routinely.

All standard gases are pressurized in 29.5 L treated aluminium alloy cylinders (Scott-Marrin Inc) fitted with high-purity, two-stage gas regulators. An automated sampling module equipped with a VICI 8 port multi-position valve is designed to sample from separate gas streams (standard tanks and ambient air) at each of the station. The three standards are analysed by the system every 6 to 12 hours. Similarly, the flask measurements in Beijing lab are also linked to the WMO/GAW standards to guarantee the comparability.

Quality assurance and quality control All the measurements used in this study are provided under the framework of WMO/GAW Programme. To check the system performance at each station a calibrated cylinder filled with compressed ambient air is used as a target gas (T) to check the precision and stability of the system routinely. The bias between the assigned and measured value is evaluated and accepted when it is less than ±0.2 ppm. Otherwise, the ambient measurements are flagged as invalid, and no longer considered. Figure S2 shows examples of the bias at four of our stations. For the flask measurements analysed in our Beijing laboratory, we apply similar strategy to check the analytical quality.

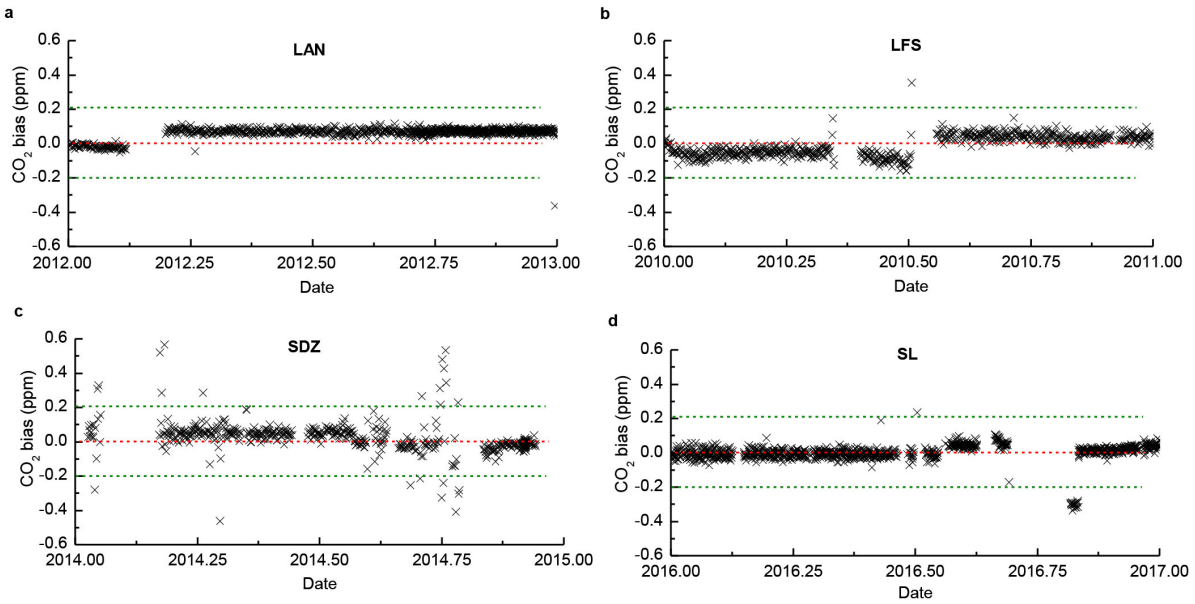

Figure S2 Typical examples of measurement bias relative to target measurements. Bias is described here as the difference between the assigned and the measured values for the target gas cylinders.

As a member of WMO/GAW programme we are obligated to participate in all comparison/audit activities sponsored by WMO/GAW to guarantee that our measurements continue to meet the goals of WMO/GAW. For example, results from the latest GAW round-robin (https://www.esrl.noaa.gov/gmd/ccgg/wmorr/) and the GAW World Calibration Centre (WCC) audit (https://www.empa.ch/documents/56101/250799/LAN_MOC_2016.pdf/e6d6ed18-f318-47f0-a6d2-60f272bf9845) indicate that the *in situ* measurements used in this study meet the goals of WMO/GAW. Figure S3 shows an example of the CO_2 measurements audited at the LAN station, with bias reported between our measurements and the GAW WCC standards for six travel standards.

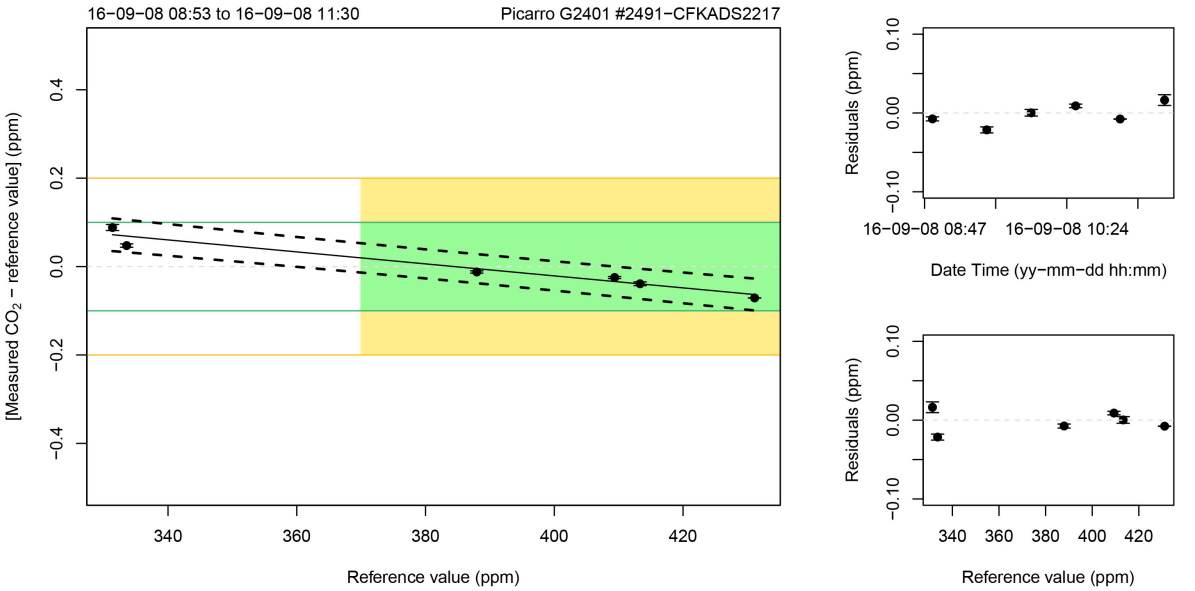

Figure S3 Audited CO_2 measurements at LAN station in China. Over the tested CO_2 mole fraction range, the measurements at LAN meet the ±0.1 ppm compatibility

goals of WMO/GAW denoted by the green shaded region; the yellow shaded regions shows the extended goal. This figure is adapted with permission from the audit report of WMO/GAW WCC: https://www.empa.ch/documents/56101/250799/LAN_MOC_2016.pdf/e6d6ed18-f318-47f0-a6d2-60f272bf9845.

Data processing Because of the dead volume in the plumbing of the *in situ* system, the response of the system is not stable until one minute after switching to a different gas source using the multi-position valve. Acknowledging this, we sequentially connect every standard gas cylinder to the system for 5 minutes. Consequently, the raw ambient data are separated into 5-minute segments. The concentration routine discards the first 3 minutes of data and only uses the mean of the last 2 minutes to calculate the concentration through the latest linearity regression factors. Because the CRDS system measures every 2-3 seconds, the number of measurements in the last 2 minutes is sufficient to represent the conditions in identical 5 minutes segments. Invalid data caused by instrumental malfunction are checked with information from the station logbook. After computing CO_2 mole fractions, the data are manually inspected. Occasionally, information in the station logbook identifies periods when measurements are affected by analytical or sampling problems including poor instrument performance or local influences such as nearby fires, vehicles, and cattle. After these steps, all of the 5-minute data are combined into hourly averages that we use in our study.

Data filtering The CO_2 observations at the sites are unavoidably influenced by local sources and sinks. Identification of regionally-representative CO_2 measurements that are minimally influenced by local anthropogenic emissions or land biosphere is therefore essential. To distinguish the CO_2 observations influenced by anthropogenic emissions adjacent to a station (villages, traffic emissions, etc.) and local vegetation canopy (field, forest, etc), as used in previous studies (Fang et al., 2014, 2015), we filter the hourly CO_2 observations by considering the meteorological factors, local topography, and anthropogenic activities.

We employ a three-stage data filtering process. First, we only use data during daylight hours, e.g. 10:00 to 16:00 (local time) at LAN and from 09:00 to 16:00 (local time) at LFS and SDZ, which have better representative conditions. Measurements of CO_2 at LAN station from two levels (10 and 50 m a. g. l.) have shown that the vertical difference between the two levels is minimum (less than 0.2±0.2 ppm) between 10:00 and 16:00 and is stable. Thus, the data during this period of the day are selected when the boundary layer is high and the vertical mixing is strong (e.g., Figure S4 for LAN and LFS stations). For other stations, we apply a similar method.

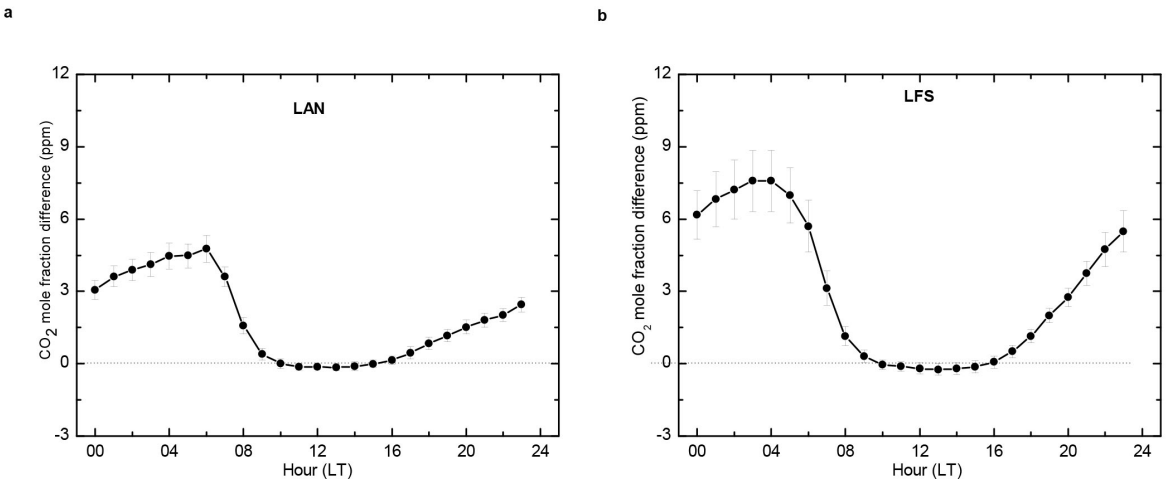

Figure S4 Example of diurnal differences of hourly CO_2 mole fractions between the 10 m and the top of each tower at **a** LAN and **b** LFS station. Error bars denote confidence intervals of 95%.

Second, guided by nearby potential contamination sources, CO_2 observations are determined to be locally representative when surface winds prevail from adjacent local sources/sinks such as villages, factories, and paddy rice fields. The rejected wind sectors (local representative) are flagged in four seasons at all of the stations. For example, the data when local surface winds are from SSW-SW and N sectors are flagged at LAN station to exclude the transports from the Lin'an town located at 6 km southwest and the small factory (north of the station, 1.4 km away), where charcoal is manufactured from burning bamboo wood.

Finally, to minimize the influence of very local sources and sinks, the remaining data is filtered by discarding data when the local surface wind speed is lower than 1.5 m s^{-1} (Beaufort scale 0 and 1). For the WLG station, we also flag the CO_2 records when the wind speed is higher than scale 6 (>10.8 ms^{-1}), because the higher wind speed may also transport emissions from much broader regions (e.g., Xining and Lanzhou) at WLG. After our three-step filter, the resulting hourly data is considered to be regionally representative and are used in our study.

For the discrete flask samples at JS and AKDL, anomalous data caused by improper sample collection operations (Lang et al., 1990) or error in analysis (flagged by QC), are discarded. When the difference between pair samples is larger than 0.4 ppm, corresponding to three times the mean pair agreement, we consider one or both flasks are contaminated and discard the measurement. After this processing, the means of flask sample pairs are used in this study.

Extended Data Figure 1 shows the hourly/weekly mean observations from the sites we use across China. We use some flask observations to fill gaps left by the CRDS system in SL.

GOSAT and OCO-2 Satellite Observations

We use column CO_2 data collected by the Japanese Greenhouse gases Observing SATellite (GOSAT) and the NASA Orbiting Carbon Observatory (OCO-2). GOSAT was launched in January 2009 in a 666-km altitude sun-synchronous orbit with a local overpass time over China around 13:00 in its descending node (Kuze et al,

2016). OCO-2 was launched on July 2, 2014 and inserted into the front of the 705-km Afternoon Constellation (A-Train) on August 3, 2014. It has a mean local overpass time of 13:36 in its ascending node and has a 16-day (233-orbit) ground-track repeat cycle (Crisp, 2015). Recent work has shown that radiance measurements from earlier versions of these independent datasets (ACOS-GOSAT B7.3 and ACOS-OCO2 B7) are generally within 5% for all bands when they view the same scene at the same time (Kataoka et al, 2017).

The GOSAT Thermal And Near-infrared Sensor for carbon Observation (TANSO) comprises two instruments: a Fourier Transform Spectrometer (FTS) and the Cloud and Aerosol Imager. The FTS observes five across-track nadir pixels (three across-track pixels after August 2010) with a footprint diameter of 10.5 km, an across-track spacing of about 100 km, and an along-track spacing of 90–280 km. This results in an approximate three-day revisit time. We use the column-averaged dry air mole fraction of atmospheric CO_2(X_{CO2}) full-physics retrievals from v7.3 data (downloaded from GES DISC/GOSAT) product from the Atmospheric CO_2 Observations from Space (ACOS) from the Jet Propulsion Laboratory (JPL, O'Dell et al., 2012).

OCO-2 comprises three imaging grating spectrometers for three bands: two shortwave infrared CO_2 bands and an O_2 band (Crisp et al.,2008). The OCO-2 employs three observation modes: nadir, sun glint (specular reflection), and target. For routine science operations, OCO-2 either points the instrument boresight to the local nadir or towards sun glint. The spatial resolution of individual measurements is < $3km^2$ (Eldering et al., 2017). We use ACOS v8r OCO-2 X_{CO2} data (O'Dell et al.,2018) for this work (downloaded from GES DISC/OCO-2).

Extended Data Figure 4 shows the spatial coverage of clear-sky X_{CO2} data observed by GOSAT over China during December 2014 to November 2015. It shows a seasonal dependence, mainly reflecting changes in solar zenith angle and cloud coverage. There are very few data in winter over the northern part of China. Extended Data Figure 4 also shows that for the same period there are many more clear-sky observations from OCO-2, reflecting the smaller ground footprint of OCO-2 measurement.

2 Atmospheric Transport Model and ensemble Kalman Filter

We use the GEOS-Chem global chemistry transport model (v9.02, http://acmg.seas.harvard.edu/geos/index.html) to relate *a priori* surface fluxes to atmospheric CO_2 observations. We run the model at a spatial resolution of 4^o latitude by 5^o longitude and 47 vertical levels, driven by GEOS-5 (2009-2012) and GEOS-FP (2013-2016) meteorological analyses from the Global Modeling and Assimilation Office at NASA Goddard Space Flight Centre. We use *a priori* flux inventories to describe: monthly fossil fuel emissions, (Oda and Maksyutov, 2011); weekly biomass burning emissions (van der Werf et al., 2010); climatological monthly oceanic surface fluxes (Takahashi et al., 2009), and three-hourly terrestrial biosphere-atmosphere fluxes (Olsen and Randerson, 2004).

We use an ensemble Kalman filter (Feng et al., 2009, 2011, 2017) to infer *a posteriori* surface CO_2 fluxes from atmospheric CO_2 data. We estimate monthly fluxes on a spatial distribution based on TransCom-3 (Gurney et al., 2002) with each continental and ocean region further divided into sub-regions. On the global scale, we estimate fluxes for 475 land regions and 317 ocean regions (totally 792 regions, Figure S5) for each month between January 2009 and December 2016, resulting in a state vector length of 76,032. Over China, we infer fluxes at the spatial resolution of the atmospheric transport model, corresponding to 58 geographical regions. We discuss below the role of flux error correlations between neighbouring grid points.

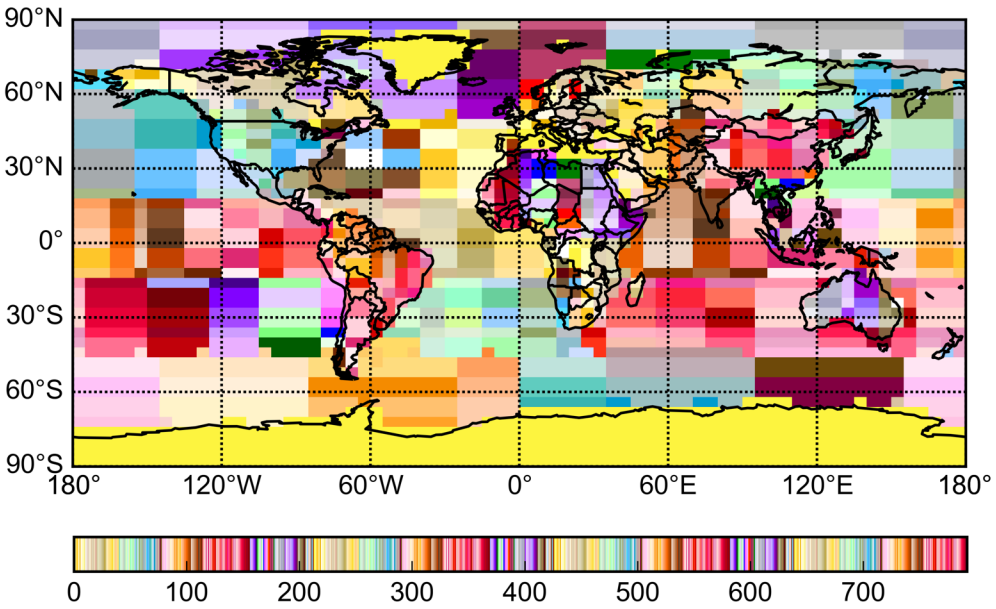

Figure S5 A map of the 792 geographical regions used in our inversions.

Here, we outline the approach we use to estimate annual uncertainty estimates from the ensemble Kalman filter with a lagged window. This approach provides a simple approximation for estimating the uncertainty in multi-year *a posteriori* flux estimates. It is based on the assumption that direct temporal error correlations are introduced by sharing the same observation constraints, and hence they are relatively small when the time gap is larger than the lag window. This approach retains the correlations within our 4-month lag window while propagating indirect correlations step-by-step through overlaid months of the moving lag window.

Following the sequential data assimilation theorem, observations for the whole experiment period are assimilated sequentially monthly. *A posteriori* estimates from each step are used as the *a priori* to assimilate observations in the following month. By assimilating observations at month *i*, we obtain the *a posteriori* error covariance $\mathbf{P}_i^a$:

$$\mathbf{P}_i^a = (\mathbf{I} - \mathbf{K}_i\mathbf{H}_i)\mathbf{P}_i^f, \quad (1)$$

where $\mathbf{H}_i$, a subset of the full Jacobian **H**, projects flux estimates corresponding to month *i* to observation space, and the Kalman gain matrix $\mathbf{K}_i$ for step *i* is determined by

$$\mathbf{K}_i = \mathbf{P}_i^f \mathbf{H}_i^T [\mathbf{H}_i \mathbf{P}_i^f \mathbf{H}_i^T + \mathbf{R}_i]^{-1}, \quad (2)$$

where $\mathbf{R}_i$ represents the observation error covariance subset for month *I*. $\mathbf{P}_i^f$ is the *a priori* flux for step *i*, which is the *a posteriori* error covariance from step *i-1*. We have assumed individual observations are independent.

We now introduce flux perturbation matrices, $\Delta\mathbf{X}_i^f$ and $\Delta\mathbf{X}_i^a$, as the square root of *a priori* and *a posteriori* error covariances, respectively: $\mathbf{P}_i^f = \Delta\mathbf{X}_i^f (\Delta\mathbf{X}_i^f)^T$, and $\mathbf{P}_i^a = \Delta\mathbf{X}_i^a (\Delta\mathbf{X}_i^a)^T$. As a result, we can re-write Eq. 2 as:

$$\Delta\mathbf{X}_i^a (\Delta\mathbf{X}_i^a)^T = \Delta\mathbf{X}_i^f [\mathbf{I} - \Delta\mathbf{Y}_i^T (\Delta\mathbf{Y}_i^T \Delta\mathbf{Y}_i + \mathbf{R}_i)^{-1} \Delta\mathbf{Y}_i] (\Delta\mathbf{X}_i^f)^T, \quad (3)$$

where $\Delta\mathbf{Y}_i = \mathbf{H}_i \Delta\mathbf{X}_i^f$ represents the spread of the model concentration values as the response to flux perturbation matrix $\Delta\mathbf{X}_i^f$. Following the Ensemble transform Kalman filter approach (Bishop et al., 2001), we introduce a transform matrix $\boldsymbol{\alpha}_i$:

$$\boldsymbol{\alpha}_i (\boldsymbol{\alpha}_i)^T = [\mathbf{I} - \Delta\mathbf{Y}_i^T (\Delta\mathbf{Y}_i^T \Delta\mathbf{Y}_i + \mathbf{R}_i)^{-1} \Delta\mathbf{Y}_i], \quad (4)$$

allowing us to rewrite Eq. 3 as:

$$\Delta\mathbf{X}_i^a (\Delta\mathbf{X}_i^a)^T = (\Delta\mathbf{X}_i^f \boldsymbol{\alpha}_i)(\Delta\mathbf{X}_i^f \boldsymbol{\alpha}_i)^T = \Delta\mathbf{X}_{i+1}^f (\Delta\mathbf{X}_{i+1}^f)^T, \quad (5a)$$

or

$$\Delta\mathbf{X}_{i+1}^f = \Delta\mathbf{X}_i^a = \Delta\mathbf{X}_i^f \boldsymbol{\alpha}_i \ . \quad (5b)$$

As shown in Eqs. 4 and 5, the transform matrix, $\boldsymbol{\alpha}_i$ mainly reduces the spread of the flux perturbation matrix due to the assimilation of observations at month *i*. However, $\boldsymbol{\alpha}_i$ is usually non-diagonal, with off-diagonal values representing contributions to $\Delta\mathbf{Y}_i$ from flux perturbations at different time and locations even though we assume $\mathbf{R}_i$ is diagonal.

After repeating the above steps to assimilate observations through the whole experiment period of *m* months, we obtain the final *a posteriori* error covariance:

$$\mathbf{P}^a = \Delta\mathbf{X}_m^a (\Delta\mathbf{X}_m^a)^T = (\Delta\mathbf{X}_0 \boldsymbol{\alpha}_t)(\Delta\mathbf{X}_0 \boldsymbol{\alpha}_t)^T, \quad (6)$$

where the final transform matrix $\boldsymbol{\alpha}_t$ is calculated iteratively by propagating from month *i*=1 to m:

$$\boldsymbol{\alpha}_t = \prod_{i=1}^{m} \boldsymbol{\alpha}_i. \quad (7)$$

With the exception of our assumption of independent observations, no explicit approximation has been introduced in Eqs. 6 and 7 for determining the full *a posteriori* error covariance. However, we have a total of 76032 (8 years x 12 months x 792 regions) variables. Any direct numerical computation using Eqs.6 and 7 would be very expensive, partially because the projection of the flux perturbations to the

observation space (i.e., $\Delta\mathbf{Y}_i \sim \mathbf{H}_i \Delta\mathbf{X}_i^f$) also involves atmospheric modelling of tracer transport using a global 3D chemistry transport model.

In our study, we use a moving lag window of 4 months to reduce computational cost. This is a common approach that assumes that observations at one time provide only weak constraints on past fluxes on time periods longer than 4 months, i.e. contributions are too dilute. It reduces the effective variable number to 3168 (4 months x 792 regions) within each assimilation window, so that the corresponding transform matrix $\boldsymbol{\alpha}_i^w$ has a much reduced dimension of 3168×3168, even when a full representation of the perturbation matrix is used (Feng et al., 2009, 2016). Further, the windowed transform matrix $\boldsymbol{\alpha}_i^w$ is one of the step-by-step outputs explicitly estimated in our current study based on an ensemble approach (Feng et al., 2009, 2016).

During post-processing, we use Eq. 7 to propagate the individual transform matrices $\boldsymbol{\alpha}_i^w$ in to the final *a posteriori* error covariance (Eq. 6). Constraint by observations on flux estimates outside their lag window is relatively weak and we ignore those contributions. As such, we can approximate the full-size $\boldsymbol{\alpha}_i$, which describes the impacts on the full flux estimate uncertainty by observations at month *i*, by assuming:

$$\boldsymbol{\alpha}_i \approx \begin{bmatrix} \mathbf{I}_{1,i-4} & \mathbf{0} & \mathbf{0} \\ \mathbf{0} & \boldsymbol{\alpha}_i^w & \mathbf{0} \\ \mathbf{0} & \mathbf{0} & \mathbf{I}_{i+1,n} \end{bmatrix}, \quad (8)$$

where $\mathbf{I}_{1,i-3}$, and $\mathbf{I}_{i+1,n}$ are identity matrices for preceding months 1 to *i*-4, and for the subsequent months *i*+1 to *n*, respectively. By applying the (approximated) full size $\boldsymbol{\alpha}_i$ for each step to Eq. 7, we are able to construct the final transform matrix $\boldsymbol{\alpha}_t$. Together with the assumed *a priori* flux perturbation $\Delta\mathbf{X}_0$, we can then estimate the full *a posteriori* error covariance via Eq. 6, enabling us to calculate aggregated uncertainty for selected region and time period.

Our reported uncertainty for annual mean regional flux estimates should be considered as underestimates. Similar to alternative methods of estimating *a posteriori* errors, we are subject to the accuracy of often poorly quantified errors that describe the *a priori* and the atmospheric transport model.

3 Results

The impact of *in situ* data on understanding Chinese CO_2 fluxes

We use a simple error metric to determine the improvement in our understanding of Chinese CO_2 fluxes from using the additional data over Siberia and China: $\gamma = 1 - \sigma^a/\sigma^f$ (Palmer et al, 2000), where σ^a and σ^f denote the *a posteriori* and *a priori* variance uncertainties, respectively.

Figure S6 shows that the γ metric from the NOAA/ESRL and the additional reduction from using the JR-STATION and Chinese data. We find that the Siberian data improve CO_2 fluxes over most of boreal Eurasia, including the geographical region immediately upwind of China. This allows the new Chinese data to constrain flux estimates across China, as we report in detail below.

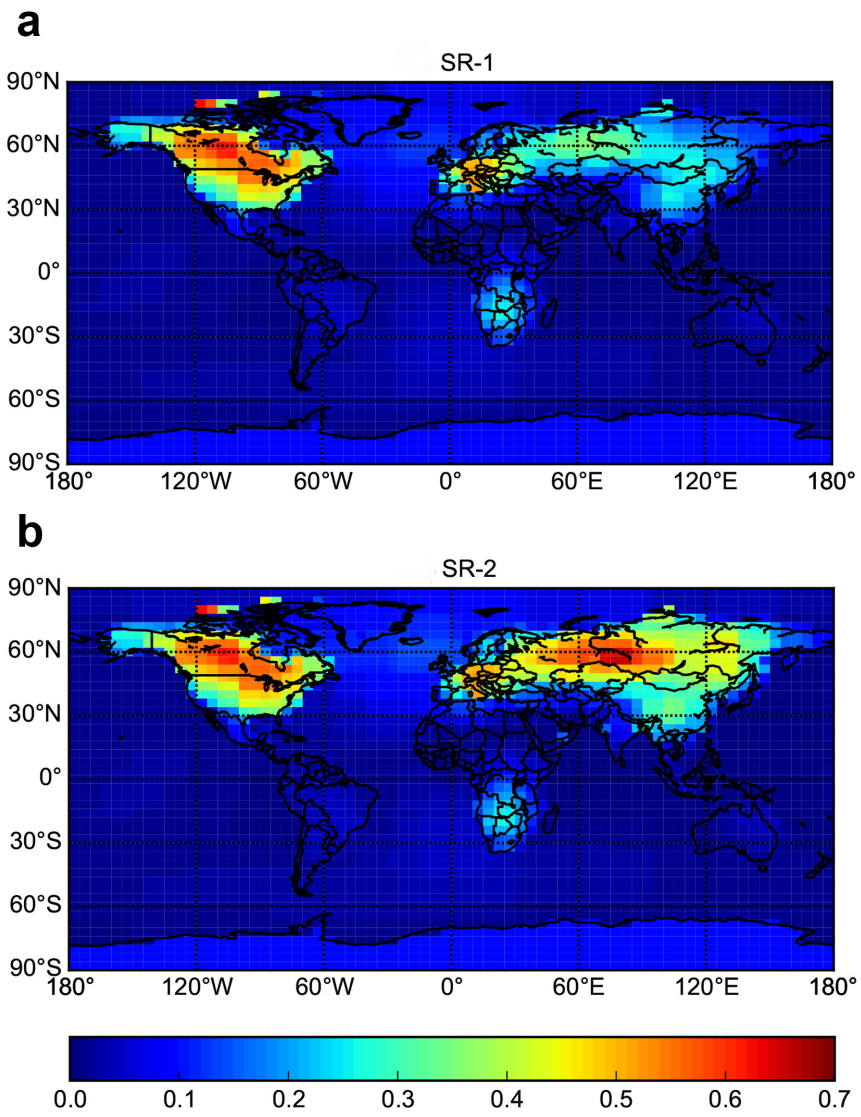

Figure S6 Example error reduction (γ metric) for April 2011. Top panel shows the γ metric after ingesting NOAA/ESRL ObsPack data (inversion SR-1, see main paper), and the bottom panel shows the γ metric after ingesting ObsPack + JR-STATION + WDCGG and CMA data (inversion SR-2). Higher γ values denote a larger reduction in flux uncertainties.

<u>Seasonal difference between SR-1 and SR-2 inversions</u>

Figure 1 shows that inversion SR-1 generally underestimates the annual uptake in Southwest China and the emission over eastern and northern China (north of 30°N, east of 110°E).

Figure S7 shows that the seasonal SR-2 minus SR-1 differences averaged over 2010-2016. We find that the SR-1 underestimates uptake in Southwest China throughout the year, and underestimates uptake in Northeast China mainly during summer months. This is further discussed below when we report changes in leaf phenology. We also find that SR-1 underestimates net emissions over eastern and northern China (38-54°N, 115-135°E) during spring, autumn, and winter months.

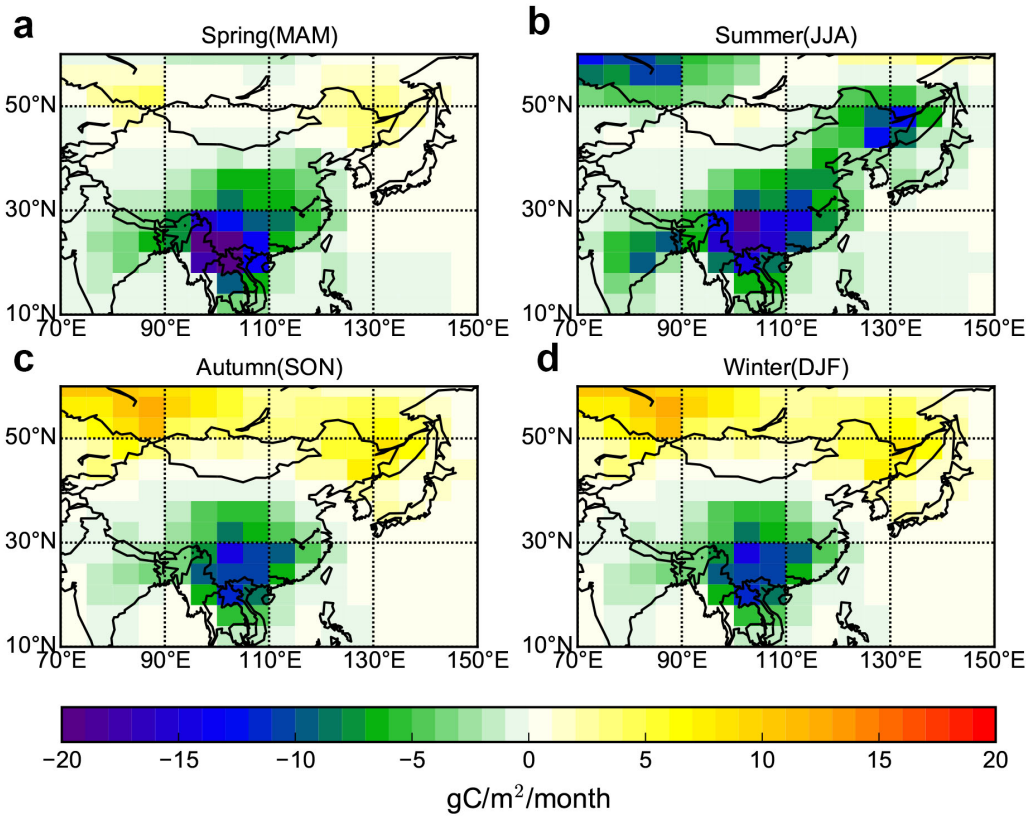

Figure S7 Seasonal mean differences of SR-2 minus SR-1 inversions during 2010-2016 (gC/m^2/month).

Sensitivity of land biosphere fluxes to assumed *a priori* anthropogenic emissions

Our inverse model calculations estimate the net CO_2 flux. We determine the land biosphere flux by subtracting emission estimates from fossil fuel combustion and cement production. This is a common approach (Peylin et al., 2013; Thompson et al.,2016; Jiang et al.,2016), based on an assumption about our knowledge of fossil fuel emissions. Consequently, our biosphere fluxes depend on what we assume for anthropogenic emissions.

Here, we report a range of China fossil fuel flux estimates using inventories from the Carbon Dioxide Information Analysis Center (CDIAC, Boden et al., 2017); Emissions Database for Global Atmospheric Research (EDGAR V4.3.2, Janssens-Maenhout et al., 2017); International Energy Agency (IEA, 2017); Liu et al., (2015); Shan et al., (2018); and the Open-Data Inventory for Anthropogenic Carbon dioxide (ODIAC, 2016). The data published by CDIAC, EDGAR and ODIAC are similar and larger than the data from IEA, 2017 and Liu et al (2015) (Table S3). We scale ODIAC emissions over China by 88% for our control run, guided by recent Chinese sectoral emission estimates from Shan et al., (2018). We retain the seasonal and spatial distributions of ODIAC emissions over China.

	CDIAC	EDGAR	IEA	Liu	Shan	ODIAC	88% ODIAC
2010	2.48	2.52	2.25	2.11	2.16	2.49	2.19
2011	2.74	2.75	2.48	2.28	2.39	2.75	2.42
2012	2.82	2.81	2.52	2.43	2.48	2.82	2.48
2013	2.88	2.93	2.63	2.50	2.60	2.92	2.57
2014	2.90	2.97	2.64		2.58	2.93	2.58
2015	2.87	2.94	2.64		2.53	2.92	2.57
2016	2.87	2.93				2.92	2.57

Table S3 Annual Chinese estimates of fossil fuel and cement production (PgC/yr) from 2010 to 2016.

A priori annual fossil fuel emissions for China, taken from the ODIAC inventory, represent 2.49-2.93 PgC/yr. As described above, for our control run we use 88% of the ODIAC emission estimates, so the fossil fuel emissions are 2.19-2.58 PgC/yr. Including fluxes from the ocean, biomass burning, and the land biosphere (section 2) results in a net *a priori* flux of 2.33-2.61 PgC/yr.

Results and comparison with previous studies

Table S4 shows our annual mean *a posteriori* land biosphere CO_2 uptake for SR-1 and SR-2 are -0.66±0.52 PgC/yr and -1.11±0.38 PgC/yr, respectively, during 2010-2016. In comparison, *a posteriori* land biosphere CO_2 uptake estimates inferred from GOSAT-ACOS are -0.83±0.47 PgC/yr and -1.10±0.43 PgC/yr during 2010-2015 and 2015-2016, respectively, crudely separating year to account for the 2015/2016 El Niño.

As noted in the main paper (Table 1), our SR-2 estimate for the land biosphere uptake of CO_2 inferred from the new CMA *in situ* data (section 1) is higher than previous estimates. Piao et al (2009) used biomass and soil carbon inventories extrapolated by satellite observations of leaf phenology, process-based ecosystem models, and atmospheric inversions to infer independent CO_2 flux estimates that range from -0.19 to -0.26 PgC/yr for Chinese terrestrial ecosystems over the 1980s and 1990s. They attributed 65% of this carbon sink to southern China due to regional changes in climate, large-scale reforestation and shrub recovery. Tian et al (2011) used a process-based ecosystem model driven by meteorological and atmospheric composition data and by knowledge of regional land use and management practices. They estimated a Chinese CO_2 sink of -0.179 PgC/yr with a 95% confidence range from -0.062 PgC/yr to 0.264 PgC/yr. Wang et al (2015) used climate data, spatial distributions of ecosystems, and social statistics to infer a mean Chinese terrestrial biosphere carbon sink of -0.966 PgC/yr from 2001 to 2010. Zhang et al., (2014) and Jiang et al (2016) inferred the Chinese terrestrial biosphere CO_2 sink using atmospheric data with four sites over China (WLG, LAN, LFS, SDZ). Zhang et al., (2014) estimated a mean sink of -0.33 PgC/yr over the period 2001-2010 and Jiang et al. (2016) estimated a mean sink of -0.45 PgC/yr over the period 2006-2009, ranging from -0.39 to -0.51 PgC/yr.

Other prominent studies on this topic have reported CO_2 flux estimates for East Asia, which include CO_2 terrestrial biosphere fluxes from China aggregated with those from Japan, North and South Korea and Mongolia. Piao et al (2012) used similar

approaches to those used by Piao et al (2009) but with a larger ensemble of estimates to study a longer period from 1990 to 2009. They estimated the terrestrial carbon sink for East Asia to be -0.293±0.033 PgC/yr (inventory based approach), -0.224±0.141 PgC/yr (process-based ecosystem models), and -0.270±0.507 PgC/yr (inferred from atmospheric data). Thompson et al. (2016) used an ensemble of terrestrial carbon flux estimates from several inversions to calculate a mean Asian land sink of -0.46 PgC/yr, ranging from -0.70 PgC/yr to -0.24 PgC/yr, for the period 1996-2012. They noted this sink was mostly located in East Asia where the mean CO_2 sink increased by 0.56 PgC/yr from 1996-2001 to 2008-2012.

Our results for the standard inversion SR-1 are within the range of those reported by Thompson et al (2016), as expected since they use similar data. The additional CMA data provide strong constraints on Southwest China (SR-2) where other studies have noted there is strong carbon uptake but have not had sufficient data to quantify those regional fluxes.

	A priori				SR-1	SR-2	GOSAT-ACOS	GOSAT ACOS +SR-2	OCO2-ACOS
	Total	BS	FF	$1-\sigma$	BS	BS	BS	BS	BS
2010	2.23	0.04	2.19	0.97	-0.60±0.51	-0.99±0.38	-0.60±0.46	-0.95±0.32	-
2011	2.33	-0.11	2.42	1.01	-0.74±0.53	-1.32±0.36	-0.93±0.49	-1.30±0.32	-
2012	2.49	0.01	2.48	1.01	-0.74±0.53	-1.25±0.39	-0.69±0.51	-1.12±0.34	-
2013	2.59	0.02	2.57	1.02	-0.61±0.55	-0.87±0.45	-0.88±0.47	-0.96±0.36	-
2014	2.61	0.03	2.58	0.99	-0.68±0.49	-1.08±0.39	-0.93±0.48	-1.09±0.33	-
2015	2.54	-0.03	2.57	1.03	-0.52±0.54	-1.03±0.34	-0.92±0.44	-1.02±0.31	-0.99±0.45
2016	2.58	0.01	2.57	0.93	-0.77±0.47	-1.25±0.31	-	-	-1.21±0.41
Mean	2.48	0	2.48	0.99	-0.66±0.52	-1.11±0.38	-0.83±0.47	-1.07±0.33	-1.10±0.43

Table S4 Annual mean CO_2 fluxes (PgC/yr) inferred from *in situ* and remote sensing data. *A priori* values for the total denote the sum of values from the terrestrial biosphere (BS) and fossil fuel and cement manufacture (FF). The 1-σ value uncertainty corresponds to the total value. Inversion SR-1 denotes NOAA ObsPack *in situ* data (including one site over China); inversion SR-2 denotes *in situ* data from NOAA ObsPack, Siberia, and from China; GOSAT-ACOS denotes GOSAT XCO_2 data retrieved by the ACOS team; an OCO2-ACOS denotes OCO-2 XCO_2 data retrieved by the ACOS team.

Sub-continental Chinese CO_2 flux estimates

To report sub-continental CO_2 fluxes, we divide the Chinese mainland into eight geographical regions (Extended Data Figure 2), based on land use cover and economic regions. The eight sub-regions are Northwest China (NWC), North China (NC), Northeast China (NEC), Tibet Plateau (TP), Centre China (CC), East China (EC), Southwest China (SWC) and Southeast China (SEC).

Table S5 shows that *a posteriori* CO_2 fluxes from our defined sub-continental regions are weakly correlated with neighbouring regions, with the highest values generally with adjacent regions. We also give the correlation between one Siberia region (SIB,54ºN-66ºN, 70ºE-85ºE) and eight sub-continental regions in China. The Siberia region is weakly correlated with sub-continental regions in China.

	Region	NW	North	NE	TP	CC	East	SW	SE	SIB
Jan	**NW**	+1.00								
	North	-0.062	+1.00							
	NE	-0.035	0.355	+1.00						
	TP	0.218	0.069	-0.059	+1.00					
	CC	0.040	0.388	-0.060	0.534	+1.00				
	East	-0.048	0.669	0.069	0.120	0.564	+1.00			
	SW	-0.032	0.141	-0.052	0.401	0.528	0.413	+1.00		
	SE	-0.050	0.201	-0.028	0.063	0.370	0.493	0.837	+1.00	
	SIB	-0.014	-0.077	-0.121	-0.056	-0.036	-0.017	0.0	0.006	+1.00
	Region	**NW**	**North**	**NE**	**TP**	**CC**	**East**	**SW**	**SE**	**SIB**
Jul	**NW**	+1.00								
	North	-0.049	+1.00							
	NE	-0.034	0.364	+1.00						
	TP	0.230	0.117	-0.050	+1.00					
	CC	0.039	0.383	-0.058	0.551	+1.00				
	East	-0.042	0.654	0.065	0.179	0.568	+1.00			
	SW	-0.033	0.129	-0.062	0.314	0.604	0.387	+1.00		
	SE	-0.054	0.177	-0.048	0.089	0.383	0.501	0.652	+1.00	
	SIB	-0.014	-0.078	-0.070	-0.066	-0.043	-0.025	0.001	0.001	+1.00

Table S5 *A posteriori* CO_2 flux correlation coefficients of SR-2 between neighbouring regions during contrasting months, January and July 2011.

Figure S8 shows annual net CO_2 flux estimates for each sub-continental regions shown in Extended Data Figure 2. *A posteriori* uncertainties are generally much smaller than *a priori* values, as expected, with the smallest values for the SR-2 inversion that reflects the added information from the new sites.

We find that TP and SWC are the regions which have a continuous annual net CO_2 sink over the seven study years. The large net uptake in SWC corresponds to low fossil fuel emission and high biosphere uptake in this region (Extended Data Figure 2). The other six geographical regions represent annual CO_2 emissions. The largest emissions are from EC, NC, and SEC, consistent with the population distribution and economic zones: Yangtze River Delta, Circum-Bohai Sea, and the Pearl River Delta. EC accounts for approximately 52% of net Chinese CO_2 emissions, despite significant land biosphere uptake. EC, SWC, SEC, NEC and CC are important regions for biosphere uptake, with SWC representing the largest annual value.

Extended Data Figure 2 shows the monthly mean biosphere CO_2 fluxes. For many of the regions the SR-1 inversion tracks *a priori* values throughout the year. The SR-2 inversion generally shows larger variations throughout each season compared with the SR-1 inversion. Over SWC *a posteriori* CO_2 fluxes are negative for most of the year, leading to a large, persistent annual net CO_2 uptake over this region, accounting for about 32% of the biosphere uptake over whole China.

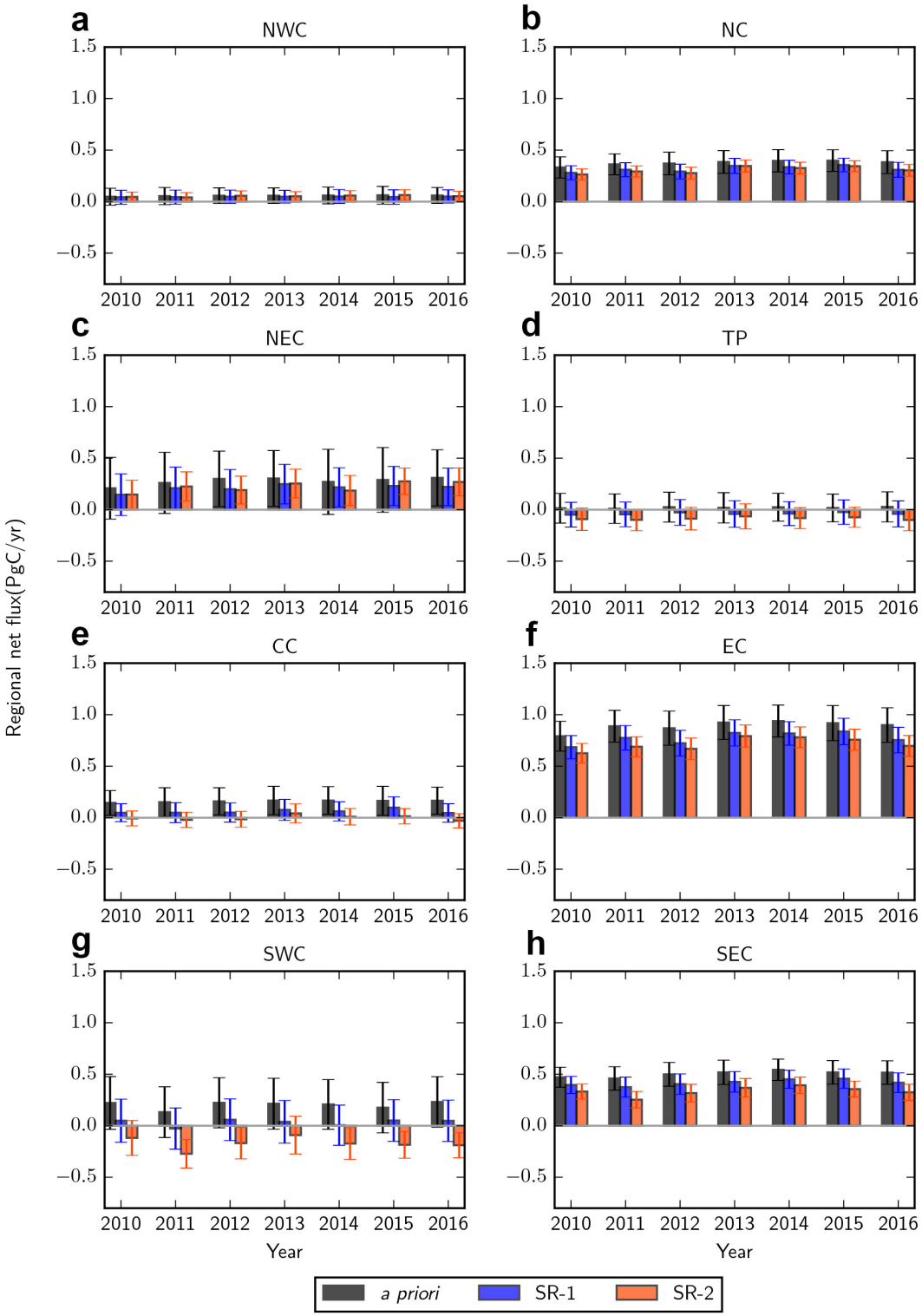

Figure S8 Annual regional *a priori* and *a posteriori* net CO_2 fluxes over China during 2010—2016. *A posteriori* fluxes are inferred from data used in SR-1 and SR-2 inversions.

Sensitivity tests

A posteriori values are reported as the mean annual estimate for period 2010-2016, inclusive.

In our assimilation of (continuous) *in situ* observations, we sample model surface CO_2 mixing ratios at the time (hour) and location of each observation and then optimally fit the resulting model daytime means with the mean observations between local time 09:00 to 16:00. Uncertainty of the mean observation is estimated by taking in account both the instrument (random) error, and the representation error that is mainly due to coarse model resolutions:

$\varepsilon_t^2 = \varepsilon_{obs}^2 + \sigma_m^2$,

where ε_{obs} is the instrument (random) error of the observation daytime mean, and σ_m represents the standard deviation between model and observed CO_2 mole fractions between 09:00 and 16:00 local time. As a result, less weight is given to observations for which (comparatively coarse) model simulations are unable to reproduce transient and small-scale variations observed by the *in situ* sites.

To further remove observations with variations that are not described by the model, we discard observations when there are fewer than three (hourly) data points in one day, or when they are far from model values (outside $3\varepsilon_t$). Similar observation quality controls have been applied in top-down studies (e.g., Chevallier et al., 2007). We used a series of sensitivity experiments (SR3 to SR6) to investigate the effect of adopting different uncertainty estimates and observation filters (Table S6). When we relax the observational filter to $5\varepsilon_t$, we infer a stronger biospheric sink: -0.85±0.50 PgC/yr (SR3) and -1.26±0.34 PgC/yr (SR4). Further relaxing the observational filter to, say, $8\,\varepsilon_t$ results in only small additional changes (<0.05 PgC/yr). When we assume a fixed observation error of 2 ppm, we infer a weaker biospheric sink: -0.68±0.52 PgC/yr (SR5) and -1.07±0.37 PgC/yr (SR6), almost the same with SR-1 and SR-2, respectively. These sensitivity tests demonstrate the qualitative robustness of the main result of the paper.

We also test the sensitivity of our *a posteriori* CO_2 fluxes to assumed *a priori* uncertainties. The inversions SR-7 and SR-8 correspond to inversions SR-1 and SR-2 but using an illustrative 20% reduction of the *a priori* uncertainty. *A posteriori* land biosphere fluxes for SR-7 (-0.55±0.45 PgC/yr) and SR-8 (-0.89±0.34 PgC/yr) are 17% and 20% weaker than values for SR-1 and SR-2, respectively, but consistent within their uncertainties. The direction of this change is as expected if we have better knowledge of the *a priori* flux estimates. The results of these sensitivity tests are also consistent with the main result of the paper.

Experiment #	**Inversion description**
SR-1	Uses NOAA obspack_co2_1_GLOBALVIEWplus_v3.2_2017-11-02 (GVI) database.
SR-2	As SR-1 and data from CMA, JR-STATION and WDCGG.
SR-3	As SR-1, but we assimilate all observations within 5 times of ε_t
SR-4	As SR-2, but we assimilate all observations within 5 times of ε_t
SR-5	As SR-1, but observation error is assumed to be a fixed value of 2 ppm.
SR-6	As SR-2, but observation error is assumed to be a fixed value of 2 ppm.
SR-7	As SR-5 but assuming 80% of a priori uncertainty.
SR-8	As SR-6 but assuming 80% of a priori uncertainty.

SR-9	As SR-1 but using ODIAC emissions from China.
SR-10	As SR-2 but using ODIAC emissions from China.
SR-11	An ensemble mean of 30 SR-2 inversions each with a random selection 5% of data removed across all sites and years.

Table S6 The inversions we present in this study.

The method we use to infer the land biosphere CO_2 flux is used widely in the community (Peylin et al.,2013; Thompson et al., 2016). First, we estimate net CO_2 fluxes by fitting our model to atmospheric CO_2 mole fraction data and then subtract fossil fuel emission estimates. Consequently, our estimate for the land biosphere CO_2 is sensitive to our assumed fossil fuel emissions. A recent study has developed a bottom-up inventory that revises downward Chinese fossil fuel emissions from 1997 to 2015 (Shan et al., 2018). In SR-1 and SR-2, we retain the spatial distribution of ODIAC fossil fuel emissions but scale the total emissions by an illustrative 88%. Comparisons between SR-1 and SR-9 and between SR-2 and SR-10, only differ by the magnitude of *a priori* fossil fuel emissions. Our land biosphere CO_2 flux for SR-1 (-0.66±0.52 PgC/yr) is 26% weaker than SR-9 (-0.89±0.52 PgC/yr), and SR-2 (-1.11±0.38 PgC/yr) is 25% weaker than SR-10 (-1.47±0.38 PgC/yr).

The CMA weekly flask and hourly continuous data we have reported represent collectively 36,939 individual points. To determine the importance of individual data points we ran estimated the carbon fluxes 30 times each with a different 5% of the data removed (SR-11). For each member of this ensemble, 1,847 randomly selected measurements (identified using a normal distribution) from across the network and across all years were removed. We find that the resulting nationwide carbon uptake estimate weakens by approximately 0.07 PgC/yr (6%) when we remove 5% of the data. The ensemble mean and median carbon flux estimate for China is -1.038 PgC/yr, ranging from -1.043 PgC/yr to -1.033 PgC/yr. The *a posteriori* flux estimates for the sub-continental regions (Figure S12) are similarly robust and approximately 6% weaker.

These results underscore the importance of being able to estimate independently fossil fuel and land biosphere fluxes of CO_2. On smaller geographical scales our *a posteriori* land biosphere fluxes for SWC are -0.35±0.15 PgC/yr (SR-2), -0.38±0.15 PgC/yr (SR-9) and -0.41±0.15 PgC/yr (SR-11), and for NEC are -0.05±0.14 PgC/yr (SR-2), -0.09±0.14 PgC/yr (SR-9), and -0.05±0.14 PgC/yr (SR-11), respectively.

Considering the results of all of our experiments, our *a posteriori* estimates for the CO_2 terrestrial biosphere uptake over China inferred using only the NOAA ESRL Obspack GLOBALVIEWplus data range from -0.55±0.52 PgC/yr to -0.89±0.52 PgC/yr. *A posteriori* estimates for the CO_2 terrestrial biosphere uptake over China that also include the CMA data range from -0.89±0.38 PgC/yr to -1.47±0.38 PgC/yr.

Evaluation

We evaluate our *a posteriori* atmospheric CO_2 values with Comprehensive Observation Network for TRace gases by AIrLiner (CONTRAIL) data and Total Carbon Column Observing Network (TCCON) data. First, we find neither data from

TCCON nor the CONTRAIL data are very sensitive to our *a posteriori* Chinese fluxes. Consequently, there is very little difference between *a posteriori* values from SR1 and SR2 and the independent data. It is because of this result that we used the satellite data as a way to evaluate the *a posteriori* fluxes (section 5) we inferred from the CMA *in situ* data.

Figure S9 shows that atmospheric CO_2 inferred from our different inversions (SR-1, SR-2 and an inversion using only GOSAT ACOS data), sampled at the location of CONTRAIL data, are very similar. This is because CONTRAIL data are not particularly sensitive to fresh Chinese outflow. Our comparison with CONTRAIL data uses exclusively ascent and descent measurements (500-900 hPa). These CONTRAIL data that recently been linked to changes in nearby upwind cities (Umezawa et al, 2020). So, variations in CONTRAIL data will also reflect changes in localized urban sources as well as larger scales relevant to our experiments.

We find that the TCCON site in Tsukuba (TK), Japan is the only TCCON site with any sensitivity to Chinese CO_2 fluxes, which is only modest. Figure S10 shows the comparison of these TCCON data and our *a posteriori* CO_2 concentrations sampled at TK. We find that our results from SR2 are only slightly better than SR1. The shift in the residual from late 2013 corresponds to a time when the Tsukuba Bruker 125HR was configured to include an additional IR channel and Si detector, allowing investigators to take correct a laser sampling error associated with the pre-processing of the GFIT spectral fitting method used in the GGG2014 data version (https://tccondata.org/2014). A laser sampling error correction that uses only the SWIR InGaAs detector spectra could help reduce the bias prior to January 2014.

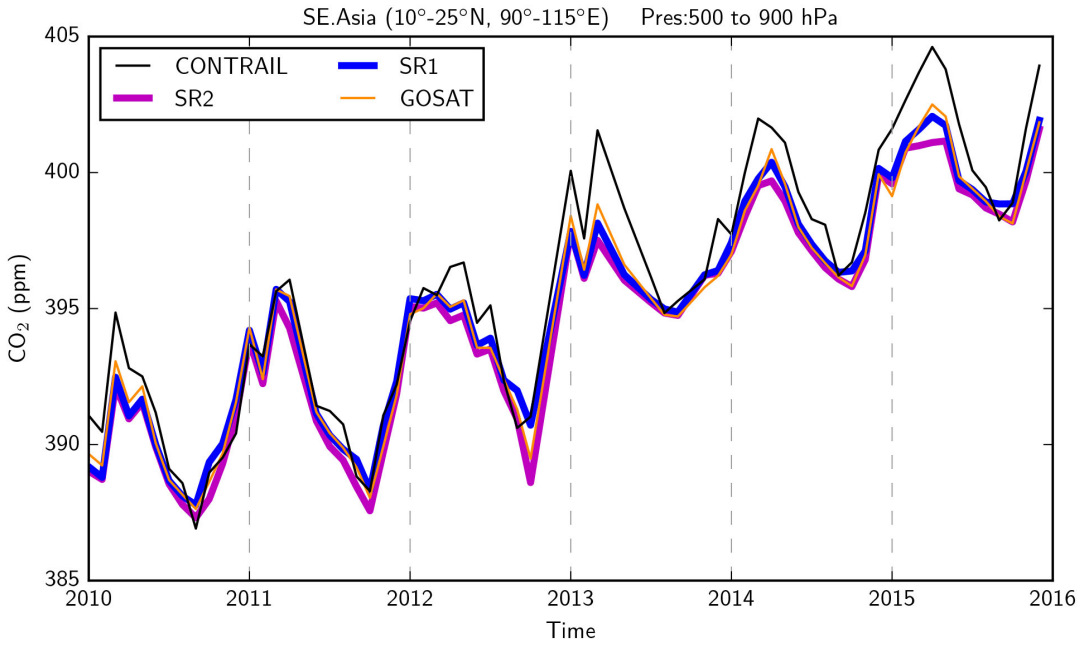

Figure S9 Comparison of *a posteriori* atmospheric CO_2 inferred from different inversions using subsets of atmospheric CO_2 mole fraction data collected over the region defined as 10°-25°N, 90°-115°E, 900-500 hPa by CONTRAIL data.

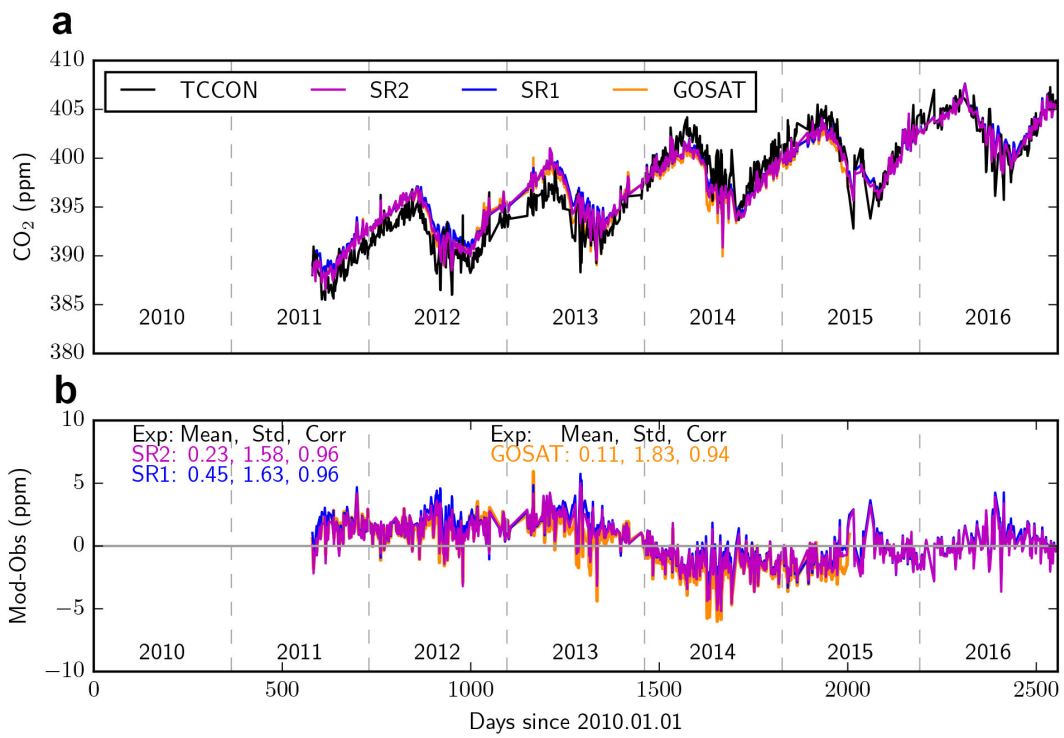

Figure S10 a Comparison of CO_2 column data observed by TCCON Tsukuba (TK) Japan and *a posteriori* atmospheric CO_2 columns inferred from different inversions that use subsets of atmospheric CO_2 mole fraction data, and **b** the corresponding model minus observation residuals.

Table S7 show select statistics of residuals between observed CO_2 mole fractions and model values corresponding to *a posteriori* flux estimates (SR-1 and SR-2). A *posteriori* CO_2 fluxes of SR-2 result in smaller mean residuals and smaller standard deviations about those means, relative to the observations compared to the SR-1 *a posteriori* CO_2 fluxes, as expected. The mean residuals of the 12 sites for SR-1 and SR-2 are -0.31 ppm and 0.04 ppm, respectively, and the corresponding standard deviations are 2.23 ppm and 2.03 ppm, respectively,

Site	Country	Location (Lat,Lon)	Obs - posterior (SR-1) mean (ppm)	Obs- posterior (SR-1) 1-σ (ppm)	Obs- posterior (SR-2) mean (ppm)	Obs- posterior (SR-2) 1-σ (ppm)
WLG	China	36.12°N,100.06°E	0	1.84	0.58	1.78
AKDL	China	47.10°N,87.93°E	1.09	2.33	1.14	1.79
JS	China,	29.63°N,114.22°E	-2.06	2.64	-1.08	2.33
SDZ	China	40.65°N,117.12°E	0.11	2.55	0.15	2.37
SL	China	28.00°N, 99.40°E	-1.59	2.56	0.56	2.30
LFS	China	44.73°N,127.60°E	0.50	3.54	0.33	2.68
LAN	China	30.03°N,119.72°E	-0.36	2.97	0.06	2.77
UUM	Mongolia	44.45°N,111.10°E	0.16	2.17	0.11	2.38

MNM	Japan	24.28°N,153.98°E	-0.14	0.90	-0.01	0.93
RYO	Japan	39.03N,141.82°E	-0.85	1.94	-1.04	1.86
TIK	Russia	71.60°N,128.89°E	0.15	0.64	0.12	0.53
DSI	Taiwan	20.70°N,116.73°E	-0.71	2.69	-0.42	2.68

673

674 **Table S7** Mean statistics of the residuals between observed and *a posteriori* CO_2
675 mole fractions. 1-σ values denote the standard deviation about the mean values.

676 4 Forest Data over China

677

678 Here, we provide a critical review of correlative remote sensing and forest census
679 data to put our result in a broader perspective. We focus on forest ecosystems
680 because they represent the largest contribution to the net terrestrial carbon sink over
681 China (Fang et al, 2007). We use satellite remote sensing data and national forest
682 inventory data to examine forest change over China.

683 Remote sensing data of forest coverage and change

684 We use the MODIS Land Cover Type Yearly Climate Modeling Grid (CMG) product
685 that has a spatial resolution of 0.05° (MCD12C1) and covers the time period 2001-
686 2012 (Friedl et al, 2010). We use the 17 land cover classes defined by the
687 International Geosphere Biosphere Programme (IGBP) global vegetation
688 classification scheme. We estimate the forest change with MODIS landcover data
689 (MCD12C1). All land cover types are classified as forest or non-forest.

690 Extended Data Figure 7 shows that most of China's forests are located in the south
691 and northeast of the country. It also shows that forest cover (from non-forest to forest)
692 has expanded considerably over the period 2001-2012, especially in SWC.

693 National forest inventories

694 China's State Forestry Administration (SFA) conducts a National Forest Inventory
695 (NFI) every five years (Zeng et al., 2015). Each survey uses established international
696 standard National forest resource continuous investigation techniques method. The
697 SFA is currently in the process of the ninth NFI (2014-2018).

698 We use survey data from the first (1973-1976) to eighth (2009-2013) forest inventory
699 data for the whole country and from the ninth forest survey for three southwest
700 provinces: Yunnan, Guangxi, Guizhou. This is summarized in Extended Data Table 1.
701 We focus on forest change on the country-scale, three provinces in SWC (Guangxi,
702 Yunnan and Guizhou), and three provinces in NEC (Heilongjiang, Jilin and Liaoning).

703 Extended Data Figure 6 show how these surveys document the increase in forest
704 coverage over China. Forest coverage in 2013 (22%) from the eighth survey has
705 doubled since the 1970s (13%) from the first survey, increasing from 121.9 to 207.7
706 million hectares with corresponding forest stocks volume increasing from 8.6 to 15.1
707 billion cubic metres. This large-scale increase, particularly since the 1990s, is due to
708 China's policy and investment on the protection of natural forest and afforestation
709 and on the recovery of natural forest and large areas of plantation forest. In particular,
710 since the start of the century forest resources have experience a period of rapid

711 growth. All provinces show an increase in forest cover with Guizhou, Guangxi, and
712 Liaoning changes the highest percentage increases.

713 We discuss data from the three most recent publicly available national surveys (6th,
714 7th, 8th) for the whole country, and also include results from the 9th survey for the
715 three southwest provinces, Guangxi, Yunnan and Guizhou (Extended Data Table 1).
716 From 1999-2013, Chinese forest area has increased by 22.2 million hectares and the
717 plantation forest area increased by 16.1 million hectares. Forest stocks have
718 increased by 2.7 billion m^3. This is due to Chinese forest protection and afforestation
719 activities from 1999 to 2013.

720 The six provinces all have high forest coverage, especially Guangxi (60%) and
721 Yunnan (59%). Yunnan and Heilongjiang have the largest forest stocks. For the
722 three northeast provinces, Heilongjiang, Jilin and Liaoning, forest stocks have
723 increased by 269.9, 106.1 and 75.7 million m^3, respectively. The increase of forest
724 stock in Heilongjiang alone accounts for 10% of the whole country's growth.

725 The subtropical forest in SWC mainly comprises of evergreen broadleaf forest on the
726 plains and coniferous forest in mountainous regions. Forest cover and forest area in
727 SWC has progressively increased, especially the area associated with plantation
728 forest. For the three provinces in Southwest China (Guangxi, Yunnan and Guizhou)
729 over the period 2000 to 2016: forest coverage has increased by 18-20%, forest land
730 area has increased by a factor of 1.4-1.8, and forest stock has increased by a factor
731 of 1.4-2.2. The increase in forest stock Yunnan alone represents 19% of the national
732 value.

733 A key factor for the rapid increase of forest in SWC is the increase of plantation
734 forests. China currently has the world's largest afforestation area (FAO, 2016). SWC
735 is one of the main regions of plantation (Huang et al., 2012). The Gunagxi
736 Autonomous Region has the largest plantation area, representing approximately 9%
737 of the total plantation within China [State Forestry Administration of the People's
738 Republic of China's, 2018]. SWC includes the eucalyptus economic forests that have
739 high growth rates. These eucalyptus forests represent 25% and 10% of planted
740 forest in Guangxi and Yunnan. The plantation forest in Guangxi, Yunnan, and
741 Guizhou accounts for a large proportion of the forest, the area proportion is 51%, 25%
742 and 51% respectively and the stock proportion is 51%, 14% and 42% respectively in
743 the 9th NFI.

744 The inventory data also show an increase of annual forest growth rate, from 3.6
745 m^3/year/ha (2003) to 4.2 m^3/year/ha (2013). Plantation forests grow more rapidly (5.5
746 m^3/year/ha) than natural forests (3.7 m^3/year/ha), the eucalyptus forest even can
747 reach to 15 m^3/year/ha. Eucalyptus in Yunnan and Guangxi account for 50% of the
748 whole country and is the second kind of plantation forest in Guangxi.

749 Another key factor that determines the magnitude of the carbon sink is the age of the
750 forest. A consequence of the rapid increase of afforestation during the last 30 years
751 is that Chinese forests contain a large fraction of young and mid-aged trees, which
752 are associated with a high rate of carbon sequestration [Pan et al., 2004; Wang et al.,
753 2011a; Yu et al, 2017]. Forests are classified as young, middle-aged, near-mature,

mature, and over-mature using distinct biological attributes, growth process, and management and utilization purpose [State Forestry Administration of the People's Republic of China's, 2018].

Extended Data Figure 9 shows that for China and the six provinces in SWC and NEC, typically 60% of forest areas are classified as young or middle-aged. In Jilin just over half of the forest area is young or middle-aged, and in Gunagxi and Guizhou over 80% of the forest areas is young or middle-aged.

Forests in Liaoning, Guizhou and Guangxi are the youngest, with 47%, 50%, and 46% classified young forest, respectively. From 1990 to 2010, forest coverage in Guizhou increased from 15% to 37%, Guangxi from 25% to 56%, and Liaoning from 27% to 38%. This reflects sustained afforestation, accompanied with high proportion of plantation forest in these three provinces. Extended Data Figure 9 shows these young forests represent only a small fraction of current forest stocks. This suggests that these young forests have still to realize their potential CO_2 sequestration capacity.

Remote sensing data of land biosphere activity

To interpret our *in situ a posteriori* CO_2 fluxes we use a variety of remote sensing data of land biosphere activity.

Leaf Area Index (LAI) is a vegetation index. It is defined as the one-sided green leaf area per unit ground area in broadleaf canopies and as half the total needle surface area per unit ground area in coniferous canopies. We use it here to track vegetation growth. We use MCD 15A2H:(MODIS/Terra+Aqua Leaf Area Index/FPAR 8-Day L4 Global 500 m SIN Grid V006) data (Myneni et al., 2015) to show the LAI information.

Normalized Difference Vegetation Index (NDVI) and Enhanced Vegetation Index (EVI) are alternative vegetative indices. They represent composite properties of leaf area, chlorophyll and canopy structure. We use MOD13C2 (MODIS/Terra Vegetation Indices Monthly L3 Global 0.05° CMG V006) (Didan et al.,2015) to get NDVI AND EVI information. The data are only retained with pixel reliability values masked as good data ("0") or marginal data ("1").

Gross Primary Productivity (GPP) is the amount of biomass that vegetation creates in a given length of time. We use it as a measure of the growth of terrestrial vegetation. The data product we use is determined on the radiation use efficiency concept. We use MOD17A2H (MODIS/TERRA Gross Primary Productivity 8-Day L4 Global 500 m SIN Grid V006) that is a cumulative 8-day composite of values with 500 metre pixel size based on the radiation-use efficiency concept (Running et al., 2015).

Net Photosynthesis (PSN) is the difference between GPP and the Maintenance Respiration (GPP-MR). The data we use are from the same files as GPP.

The MODIS data are downloaded from LP DAAC (Land Processes Distributed Active Archive Center, lpdaac.usgs.gov). The 500m resolution data are mosaicked and reprojected from the native sinusoidal projection to a geographic projection using the

MODIS Reprojection Tool (MRT). We used the MRT to re-project from the MODIS uniform grid (500m) to a geographical uniform grid (0.1°).

GOSAT Solar-Induced Fluorescence (SIF) is a measure of photosynthesis. Trees fluoresce in the range 650-800 nm, peaking at 685-690 nm and 730-740 nm. We use GOSAT SIF data retrieved using a spectral window centred on 755nm. Data are provided by University of Leicester on a regular 1°x1° grid (Somkuti et al, 2018).

Above-ground Biomass Carbon (ABC). We use ABC estimates (1993-2012) based on harmonized vegetative optical depth data for 1993 onwards derived from a series of passive microwave satellite sensors (Liu et al, 2015). These sensors include the Special Sensor Microwave Imager (SSM/I), Advanced Microwave Scanning Radiometer for Earth Observation System (AMSR-E), FengYun-3B Microwave Radiometer Imager (MWRI) and Windsat. Data are available from http://www.wenfo.org/wald/global-biomass/.

Extended Data Figure 8 shows multi-year means of these remote sensing data over China. NDVI, EVI, LAI and SIF data show values indicative of large biospheric activity over southern China (SWC and SEC) and NEC. These distributions of biospheric activity are consistent with the forest distribution showed in Extended Data Figure 7. As a result, the GPP and PSN are consistent with the distribution of NDVI, EVI, LAI and SIF. SWC has the largest PSN, which is consistent with our results shown in Figure 2 and Extended Data Figure 2. The ABC data show the above aground biomass carbon are mainly in SWC, CC and NEC, which illustrate the important role of these regions in carbon uptake in China, especially SWC and NEC.

Figure S11 show that NDVI and EVI over NEC and SWC have marginally increased from 2010-2016. NEC has a larger seasonal amplitude than SWC.

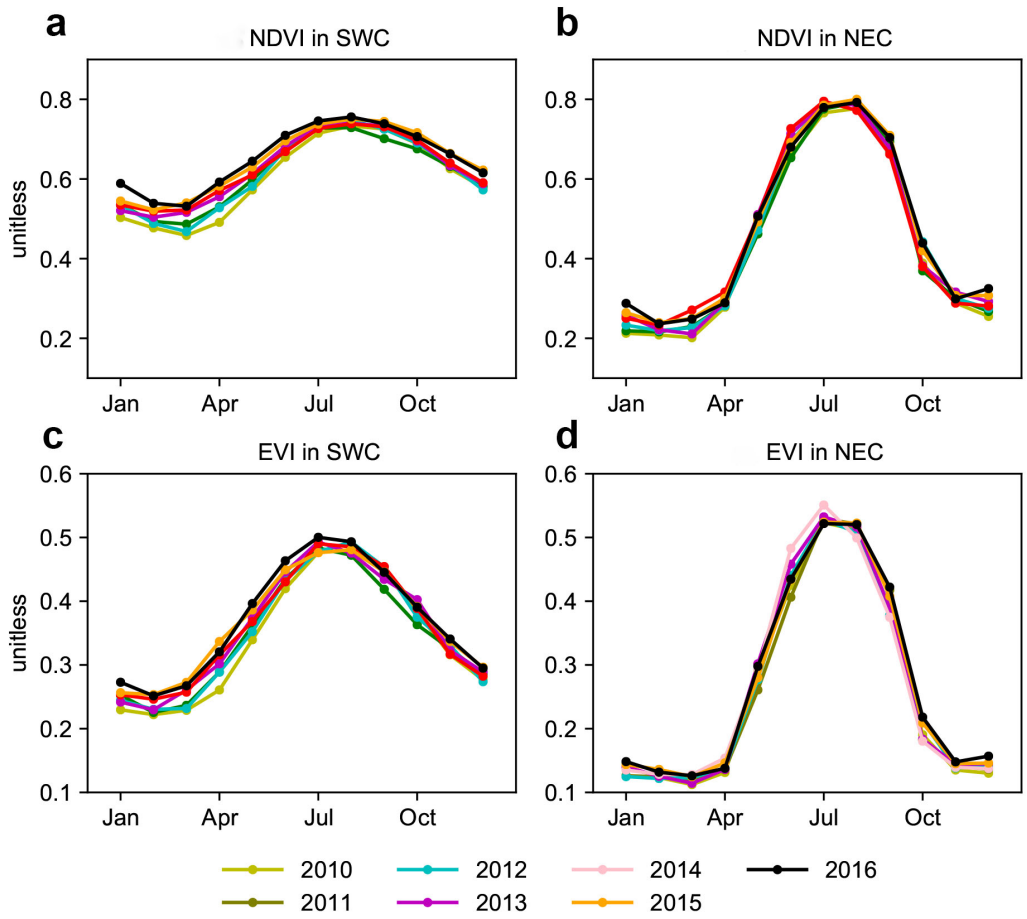

Figure S11 Seasonal variations in (top) NDVI and (bottom) EVI over (left) SWC and (right) NEC, 2010-2016.

Figure S12 shows year-to-year variations in NDVI from 2001 to 2016, including variations in the peak and trough values, mean annual values, and mean values during the growing season (April-November for SWC and SEC, and May-October for the other regions). We find a general increase of NDVI over China, especially the 'green' regions, including CC, EC, SWC, SEC and NEC. This is consistent with the increase in forest coverage over China, as discussed above. We also find that over TP, EC, SWC and SEC trough NDVI values have increased more than the peak values, resulting in a progressively dampened seasonal cycle. In contrast, over CC, NC, and NEC, we find that peak value has increased more than the trough value resulting in a larger seasonal cycle. We find similar results from our analysis of EVI (not shown).

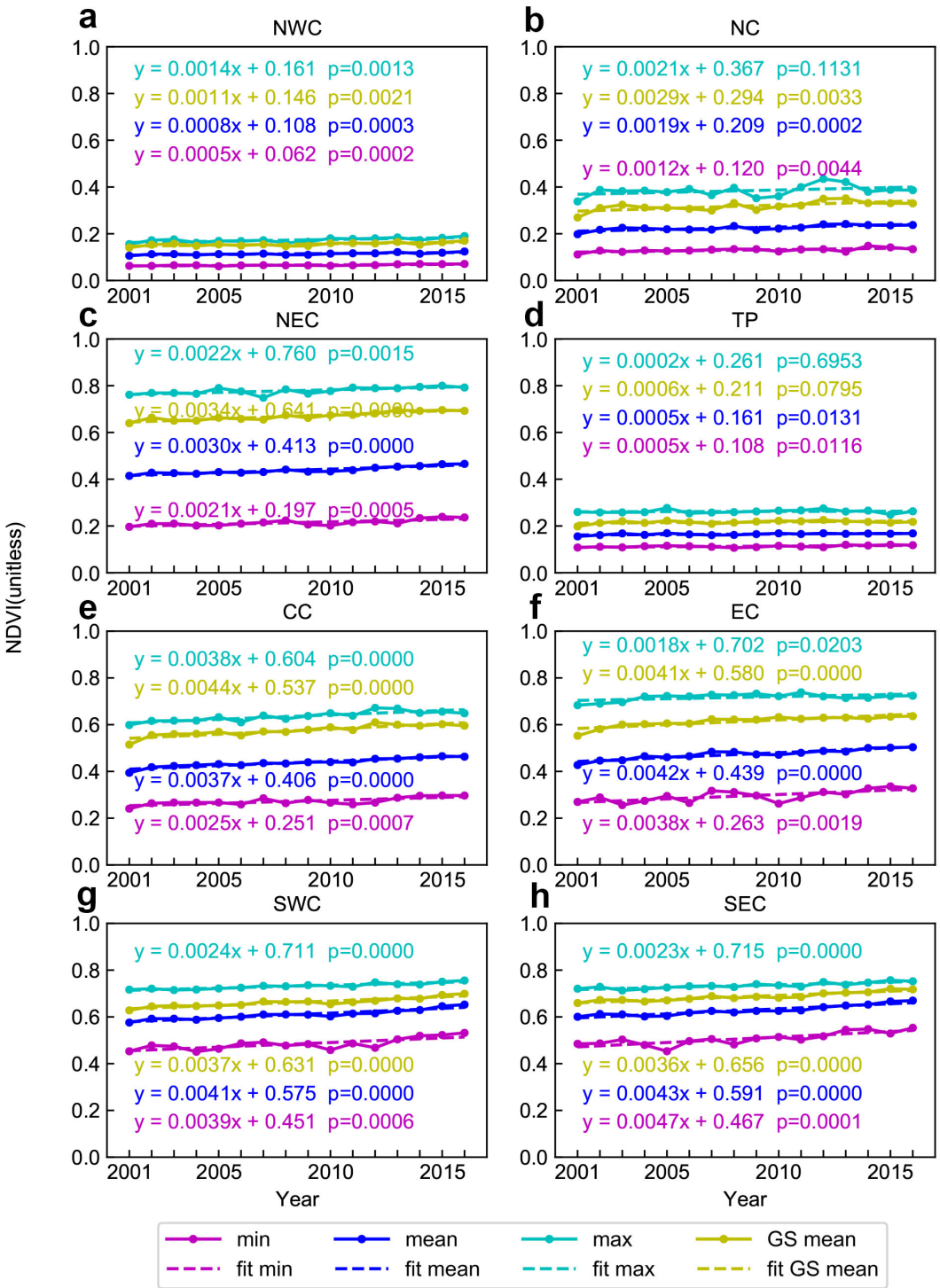

Figure S12 Year-to-year variations in NDVI over Chinese subcontinental regions (Extended Data Figure 2). Different colours denote the minimum and maximum values, mean annual value, and the mean value for the growing season. Inset is also shown the best-fit linear regression model and the associated statistical p-value.

Meteorology and hydrology measurements over SWC

We use GEOS-5 and GEOS-FP met fields to give the precipitation and temperature change in SWC (Figure S13).

Even though parts of SWC experienced two anomalous droughts during 2009-2015, autumn 2009 to spring of 2010 and during summer 2011 (Xu et al., 2015), we find an upward trend in precipitation over the broader geographical region.

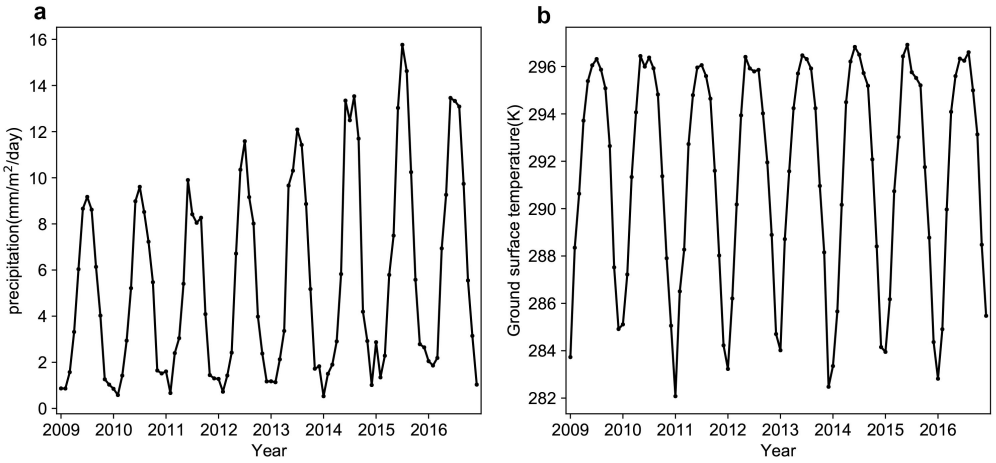

Figure S13 GEOS-5/GEOS-FP **a** precipitation rate (mm/m^2/day) and **b** surface skin temperature (K) over SWC from 2009 to 2016.

Gravity Recovery and climate experiment (GRACE) provides information about changes in the water column. Rooting depths of Chinese terrestrial ecosystems will likely be sufficiently deep that we cannot establish a direct and immediate relationship between vegetation and changes in precipitation. Changes in gravity due to changes in water column depth provide a much stronger relationship with vegetation access to water.

We use the surface mass change data based on the RL05 spherical harmonics from CSR (Center for Space Research at University of Texas, Austin), JPL (Jet Propulsion Laboratory) and GFZ (GeoforschungsZentrum Potsdam). The three different processing groups chose different parameters and solution strategies when deriving month-to-month gravity field variations from GRACE observations. We use the ensemble mean of the three data fields and multiply the data by the provided scaling grid. Data are available from http://grace.jpl.nasa.gov.

Analysis of GRACE data over SWC reveals a large seasonal cycle, determined by changes in precipitation, and a significant positive trend in the column water amount over this region. This trend also appears to be consistent with the increase in precipitation (Figure S14).

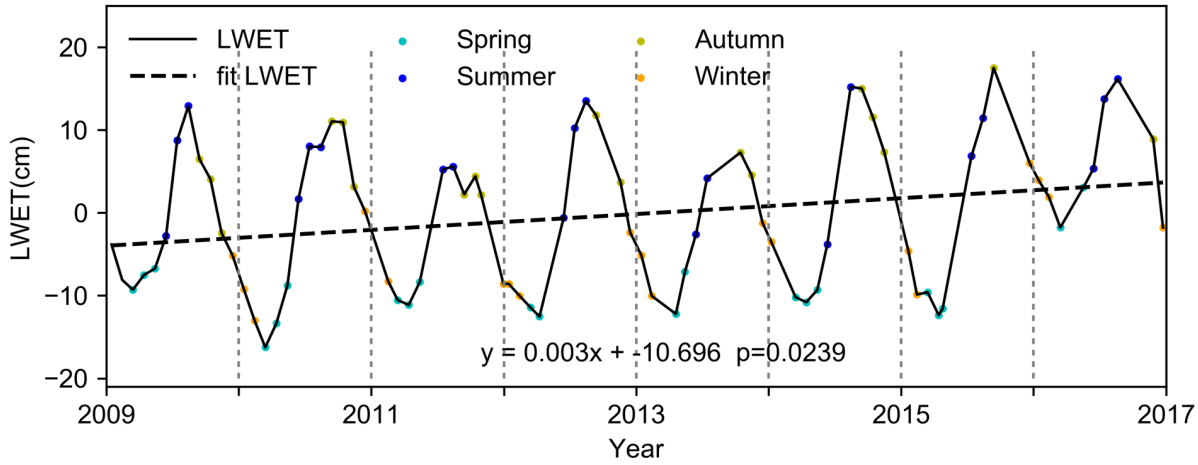

Figure S14 Anomalies in liquid water equivalent thickness (cm) inferred from the GRACE data over SWC. Anomalies are defined as the deviation from the 2004-2009 mean. The best fit regression line and the corresponding p-value are shown inset.

5 Comparison between *in situ* and satellite measurements inversion

As shown in Table 1 from the main paper, annual *a posteriori* biospheric CO_2 fluxes inferred from GOSAT and OCO-2 satellite column observations of CO_2 are less negative (smaller net sink) than annual fluxes inferred from the *in situ* (SR-2) data.

Extended Data Figure 5 shows monthly variations of the land biosphere flux inferred from *in situ* observations (inversion SR-2) and from GOSAT and OCO-2 satellite. We find that the higher annual fluxes inferred from GOSAT and OCO-2 are due mainly to higher *a posteriori* fluxes during October to April when data coverage is sparse (Extended Data Figure 4) and the fluxes are more influenced by *a priori* values.

Extended Data Figure 3 shows that mean *a posteriori* CO_2 flux distributions for May-September 2010-2015, inclusively, inferred from GOSAT and OCO-2 are consistent with the SR-2 inversion using *in situ* data. Uneven samplings during summer months (due to clouds and aerosols) result in some regional flux estimates reverting to a priori values (e.g. over the Tibetan Plateau), as expected.

6 References

Bishop, C. H., B. J. Etherton, and S. J. Majumdar, Adaptive sampling with the ensemble transform Kalman filter. Part I: Theoretical aspects, *Mon. Wea. Rev.*, 129, 420–436, doi: 10.1175/1520-0493(2001)129<0420:ASWTET>2.0.CO;2, 2001.

Boden, T.A., G. Marland, and R.J. Andres. Global, Regional, and National Fossil-Fuel CO2 Emissions. Carbon Dioxide Information Analysis Center, Oak Ridge National Laboratory, U.S. Department of Energy, Oak Ridge, Tenn., U.S.A. doi 10.3334/CDIAC/00001_V2017, 2017.

Chevallier, F., Breon, F., & Rayner, P. J. (2007). Contribution of the Orbiting Carbon Observatory to the estimation of CO2 sources and sinks: Theoretical study in a variational data assimilation framework. *J. Geophy.Res*. doi: 10.1029/2006JD007375, 2007

Cooperative Global Atmospheric Data Integration Project; Multi-laboratory compilation of atmospheric carbon dioxide data for the period 1957-2017; obspack_co2_1_GLOBALVIEWplus_v4.1_2018_10_29; NOAA Earth System Research Laboratory, Global Monitoring Division. http://dx.doi.org/10.25925/20181026, 2018

Crisp, D., Miller, C. E., & DeCola, P. L. NASA Orbiting Carbon Observatory: measuring the column averaged carbon dioxide mole fraction from space. *J. Appl. Remote Sens.*, doi: 10.1117/1.2898457, 2008.

Crisp, D. Measuring atmospheric carbon dioxide from space with the Orbiting Carbon Observatory-2 (OCO-2). Proc. SPIE 9607, Earth Observing Systems XX, 960702 (8 September 2015); doi: 10.1117/12.2187291

Crosson E R. A cavity ring-down analyzer for measuring atmospheric levels of methane, carbon dioxide, and water vapor [J]. Applied Physics B, doi: 10.1007/s00340-008-3135-y, 2008.

Didan.K. MOD13C2 MODIS/Terra Vegetation Indices Monthly L3 Global 0.05Deg CMG V006 [Terra MODIS]. NASA EOSDIS Land Processes DAAC. doi: 10.5067/modis/mod13c2.006, 2015.

Dlugokencky, E. J., Masaire, K. A., Lang, P. M., et al. A dramatic decrease in the growth rate of atmospheric methane in the northern hemisphere during 1992. *Geophys. Res. Lett,*, doi: 10.1029/93GL03070, 1994.

Dlugokencky, E.J., P.M. Lang, J.W. Mund, A.M. Crotwell, M.J. Crotwell, and K.W. Thoning (2017), Atmospheric Carbon Dioxide Dry Air Mole Fractions from the NOAA ESRL Carbon Cycle Cooperative Global Air Sampling Network, 1968-2016, Version: 2017-07-28,
Path: ftp://aftp.cmdl.noaa.gov/data/trace_gases/co2/flask/surface/.

Eldering, A., et al. The Orbiting Carbon Observatory-2 early science investigations of regional carbon dioxide fluxes. *Science*, doi: 10.1126/science.aam5745, 2017

Fang, J., Guo, Z., Piao, S., & Chen, A. Terrestrial vegetation carbon sinks in China, 1981-2000. *Sci. China. Earth. Sci.*, doi:10.1007/s11430-007-0049-1, 2007.

Fang, S. X., Tans, P. P., Steinbacher, M., Zhou, L. X., & Luan, T. Comparison of the regional CO_2 mole fraction filtering approaches at a WMO/GAW regional station in China. *Atmos. Meas. Tech*, doi:10.5194/amt-8-5301-2015, 2015.

Fang, S. X., et al., In situ measurement of atmospheric CO2 at the four WMO/GAW stations in China. *Atmos. Chem. Phys.,* doi:10.5194/acp-14-2541-2014, 2014.

FAO. 2016. *State of the World's Forests 2016. Forests and agriculture: land-use challenges and opportunities.* Rome (FAO: Food and Agriculture Organization of the United Nations). ISBN: 978-92-5-109208-8.

Feng, L., Palmer, P. I., Bösch, H., and Dance, S. Estimating surface CO2 fluxes from space-borne CO2 dry air mole fraction observations using an ensemble Kalman Filter. *Atmos. Chem. Phys.*, doi:10.5194/acp-9-2619-2009, 2009.

Feng, L., et al. Evaluating a 3-Dtransport model of atmospheric CO2 using ground-based, aircraft, and space-borne data. *Atmos. Chem. Phys.*, doi:10.5194/acp-11-2789-2011, 2011.

Feng, L, et al. Estimates of European uptake of CO2 inferred from GOSAT X_{CO2} retrievals: sensitivity to measurement bias inside and outside Europe. *Atmos. Chem. Phys.*, doi:10.5194/acp-16-1289-2016, 2016.

Feng, L, et al. Consistent regional fluxes of CH4 and CO 2 inferred from GOSAT proxy XCH4: XCO2 retrievals, 2010–2014. *Atmos. Chem. Phys.*, doi: 10.5194/acp-17-4781-2017, 2017.

Forest Resources in China, State Forestry Administration of the People's Republic of China, http://english.forestry.gov.cn/index.php?option=com_content&view=article&id=2:forest-resources-in-china&catid=10&Itemid=134 , 2018.

Friedl, M. A., et al. MODIS Collection 5 global land cover: Algorithm refinements and characterization of new datasets. *Remote. Sens. Environ.*, doi: 10.1016/j.rse.2009.08.016, 2010

Friedlingstein P, Andrew R M, Rogelj J, et al. Persistent growth of CO2 emissions and implications for reaching climate targets. *Nat. Geosci*, doi:10.1038/ngeo2248, 2014.

Fung, W. Y., Chan, S. W., Tam, K. H., and Lam, K. S. A Preliminary Analysis of Atmospheric Carbon Dioxide Concentrations in Hong Kong. *Hong Kong Meteorological Society Bulletin*, 20: 3-22, 2010.

Gurney. K. R. et al. Towards robust regional estimates of CO_2 sources and sinks using atmospheric transport models. *Nature,* doi:10.1038/415626a, 2002.

Huang L, Liu J, Shao Q, et al. Carbon sequestration by forestation across China: past, present, and future. *Renew. Sust. Energ. Rev.*, doi: 10.1016/j.rser.2011.10.004, 2012.

Janssens-Maenhout, et al., Fossil CO2 and GHG emissions of all world countries, doi:10.2760/709792, 2017.

Jiang F, et al. A comprehensive estimate of recent carbon sinks in China using both top-down and bottom-up approaches. *Sci. Rep.*, doi:10.1038/srep22130, 2016.

Kataoka et al, The cross-calibration of spectral radiances and cross-validation of CO_2 estimates from GOSAT and OCO-2, *Remote Sens.,* doi.org/10.3390/rs9111158, 2017.

Kuze, A., et al. Update on GOSAT TANSO-FTS performance, operations, and data products after more than 6 years in space. *Atmos. Meas. Tech.*, doi:10.5194/amt-9-2445-2016, 2016.

Lang, P.M., Steele, L.P., Martin, R.C., and Masarie, K.A. Atmospheric methane data for the period 1983-1985 from the NOAA/GMCC global cooperative flask sampling network. Technical memo. United States: N. p., 1990. URL: https://repository.library.noaa.gov/view/noaa/21228.

Lenton, A., Tilbrook and B., Law. Sea–air CO2 fluxes in the Southern Ocean for the period 1990–2009, *Biogeosciences*, doi:10.5194/bg-10-4037-2013, 2013.

Li, Y., et al. Reducing the uncertainty of parameters controlling seasonal carbon and water fluxes in Chinese forests and its implication for simulated climate sensitivities. *Global. Biogeochem. Cy*., doi: 10.1002/2017GB005714, 2017.

Liu, Y. Y., et al. Recent reversal in loss of global terrestrial biomass. *Nat.Clim.Change*, doi:10.1038/nclimate2581, 2015.

Liu, Z., et al. Reduced carbon emission estimates from fossil fuel combustion and cement production in China. *Nature*, doi:10.1038/nature14677, 2015.

Myneni, R. MCD15A2H MODIS/Terra+Aqua Leaf Area Index/FPAR 8-day L4 Global 500m SIN Grid V006 [Combined MODIS]. NASA EOSDIS Land Processes DAAC. doi: 10.5067/modis/mcd15a2h.006, 2015

OCO-2 Science Team/Michael Gunson, Annmarie Eldering (2016), ACOS GOSAT/TANSO-FTS ACOS Level 2 bias-corrected XCO2 and other select fields from the full-physics retrieval aggregated as daily files V7.3, Greenbelt, MD, USA, Goddard Earth Sciences Data and Information Services Center (GES DISC), Accessed: [*2017-10*], https://disc.gsfc.nasa.gov/datacollection/ACOS_L2_Lite_FP_7.3.html

OCO-2 Level 2 bias-corrected XCO2 and other select fields from the full-physics retrieval aggregated as daily files, Retrospective processing V8r, Greenbelt, MD, USA, Goddard Earth Sciences Data and Information Services Center (GES DISC), Accessed: [*2018-4*], 10.5067/XR7ZWYSKP7D0

Oda, T., Maksyutov, S. A very high-resolution (1 km× 1 km) global fossil fuel CO_2 emission inventory derived using a point source database and satellite observations of nighttime lights. *Atmos. Chem. Phys.,* doi: 10.5194/acp-11-543-2011, 2011.

O'Dell, C. W., Connor B, Bösch H, et al. The ACOS CO_2 retrieval algorithm-Part 1: Description and validation against synthetic observations. *Atmos. Meas. Tech.*, doi: 10.5194/amt-5-99-2012, 2012.

O'Dell, C. W., et al. Improved Retrievals of Carbon Dioxide from the Orbiting Carbon Observatory-2 with the version 8 ACOS algorithm. *Atmos. Meas. Tech*., doi: 10.5194/amt-2018-257, 2018.

Olsen, S. C., & Randerson, J. T. Differences between surface and column atmospheric CO_2 and implications for carbon cycle research. *J. Geophys. Res. Atmos.*, doi: 10.1029/2003JD003968, 2004.

Palmer, P. I., J. J. Barnett, J. R. Eyre, and S. B. Healy, A nonlinear optimal estimation inverse method for radio occultation measurements. *J. Geophys. Res.*, doi: 10.1029/2000JD900151, 2000.

Pan Y, Luo T, Birdsey R, et al. New estimates of carbon storage and sequestration in China's forests: effects of age–class and method on inventory-based carbon estimation. *Clim. Change*, doi: 10.1007/s10584-004-2799-5, 2004.

Peylin, P., et al. Global atmospheric carbon budget: results from an ensemble of atmospheric CO_2 inversions. *Biogeosciences*, doi:10.5194/bg-10-6699-2013, 2013.

Piao, S., et al. The carbon balance of terrestrial ecosystems in China. *Nature*, doi:10.1038/nature07944, 2009.

Piao, S. L. et al. The carbon budget of terrestrial ecosystems in East Asia over the last two decades. *Biogeosciences*, doi: 10.5194/bg-9-3571-2012, 2012.

Running, S. Mu, Q., Zhao, M. MOD17A2H MODIS/Terra Gross Primary Productivity 8-Day L4 Global 500m SIN Grid V006 [Terra MODIS]. NASA EOSDIS Land Processes DAAC. doi: 10.5067/modis/mod17a2h.006, 2015

Saeki T, Maksyutov S, Sasakawa M, et al. Carbon flux estimation for Siberia by inverse modeling constrained by aircraft and tower CO2 measurements. *J. Geophys. Res. Atmos.*, doi: 10.1002/jgrd.50127, 2013.

Sasakawa, M., et al. Continuous measurements of methane from a tower network over Siberia. *Tellus B*, doi: 10.1111/j.1600-0889.2010.00494.x, 2010.

Sasakawa, M., et al. Aircraft and tower measurements of CO2 concentration in the planetary boundary layer and the lower free troposphere over southern taiga in West Siberia: Long-term records from 2002 to 2011. *Geophys. Res. Atmos.*, doi:10.1002/jgrd.50755, 2013.

Shan, Y., et al. China CO2 emission accounts 1997-2015. Sci. Data, doi:10.1038/sdata.2017.201, 2018.

Somkuti, P., Boesch, H., Feng, L., & Palmer, P. Solar-Induced Fluorescence Response to a Regional-Scale Drought Event. Vol. 20, EGU2018-16486, 2018.

Swenson, S. C.. 2012. GRACE monthly land water mass grids NETCDF RELEASE 5.0. Ver. 5.0. PO.DAAC, CA, USA. Dataset accessed [2017-11-20] at http://dx.doi.org/10.5067/TELND-NC005.

Swenson, S. C. and J. Wahr, Post-processing removal of correlated errors in GRACE data, *Geophys. Res. Lett.*, 33, L08402, doi:10.1029/2005GL025285, 2006.

Takahashi, T., et al. Climatological mean and decadal change in surface ocean pCO_2, and net sea–air CO_2 flux over the global oceans[J]. Deep Sea Research Part II: Topical Studies in Oceanography, doi: 10.1016/j.dsr2.2008.12.009, 2009.

Tian, H., et al. Net exchanges of CO_2, CH_4, and N_2O between China's terrestrial ecosystems and the atmosphere and their contributions to global climate warming. *J. Geophys. Res. Atmos*. 116, G02011, doi:10.1029/2010JG001393, 2011.

Thompson, R. L., et al. Top–down assessment of the Asian carbon budget since the mid 1990s. *Nat. Commun*, doi:10.1038/ncomms10724, 2016.

Tomohiro Oda., Shamil Maksyutov (2015), ODIAC Fossil Fuel CO2 Emissions Dataset (ODIAC2016), Center for Global Environmental Research, National Institute for Environmental Studies, doi:10.17595/20170411.001. (Reference date: 2017/12/10)

Thoning, K. W., Tans, P. P., and Komhyr, W. D.: Atmoshperic carbon dioxide at Mauna Loa observatory 2. Analysis of the NOAA GMCC data. *J. Geophys. Res. Atmos*, 10.1029/JD094iD06p08549, 1989.

Umezawa, T., Matsueda, H., Oda, T. et al. Statistical characterization of urban CO_2 emission signals observed by commercial airliner measurements. *Sci Rep* 10, 7963, doi:10.1038/s41598-020-64769-9, 2020.

Van der Werf G R, et al. Global fire emissions and the contribution of deforestation, savanna, forest, agricultural, and peat fires (1997–2009). *Atmos. Chem. Phys.*, doi: 10.5194/acp-10-11707-2010, 2010.

Wang, S., et al. Relationships between net primary productivity and stand age for several forest types and their influence on China's carbon balance. *J. Environ. Manage.*, doi: 10.1016/j.jenvman.2011.01.024, 2011.

Wang, Q., Zheng, H., Zhu, X., et al. Primary estimation of Chinese terrestrial carbon sequestration during 2001-2010. *Sci. Bull.*, doi:10.1007/s11434-015-0736-9, 2015

Watai, T., et al. Development of an atmospheric carbon dioxide standard gas saving system and its application to a measurement at a site in the West Siberian Forest. *J. Atmos. Ocean. Tech.*, doi: 10.1175/2009JTECHA1265.1, 2010.

Xu, K., Yang, D., Xu, X., & Lei, H. Copula based drought frequency analysis considering the spatio-temporal variability in Southwest China. *J. Hydrology*, doi: 10.1016/j.jhydrol.2015.05.030, 2015.

Yu, Y., et al. Influence of site index on the relationship between forest net primary productivity and stand age. *PloS one*, doi: 10.1371/journal.pone.0177084, 2017.

Zeng, W., Tomppo, E., Healey, S. P., & Gadow, K. V. The national forest inventory in China: history-results-international context. *Forest Ecosystems*, doi: 10.1186/s40663-015-0047-2, 2015.

Zhang, H., Chen, B., Der Laanluijkx, I. T., et al. Net terrestrial CO2 exchange over China during 2001–2010 estimated with an ensemble data assimilation system for atmospheric CO_2. *J. Geophys. Res. Atmos.*, doi: 10.1002/2013JD021297, 2014

Zhao, C., P.P. Tans, and K.W. Thoning, A high precision manometric system for absolute calibrations of CO_2 in dry air. *J. Geophys. Res. Atmos*., doi: 10.1029/96JD03764, 1997.

Zhao, C. L. and P. P. Tans, Estimating uncertainty of the WMO mole fraction scale for carbon dioxide in air. *J. Geophys. Res. Atmos.*, doi: 10.1029/2005JD006003, 2006.

Zhou L X, Worthy D E J, Lang P M, et al. Ten years of atmospheric methane observations at a high elevation site in Western China. *Atmos. Environ*., doi: 10.1016/j.atmosenv.2004.02.072, 2004.

Zhou L, Conway T J, White J W C, et al. Long-term record of atmospheric CO2 and stable isotopic ratios at Waliguan Observatory: Background features and possible drivers, 1991–2002. *Global. Biogeochem. Cy*., doi: 10.1029/2004GB002430, 2005.